Available online www.jsaer.com

***Journal of Scientific and Engineering Research*, 2018, 5(5):359-394**

Research Article

ISSN: 2394-2630
CODEN(USA): JSERBR

Spectral Method Applied to Thermochemical Non-Equilibrium Reentry Flows Submitted to a Magnetic Field in 2D: Five Species

Edisson Sávio de Góes Maciel

Rua Santa Clara, 245 – Cx. Postal: 2029 – 12.243-970 – São José dos Campos – SP – Brazil

Abstract In the present work, a study involving a spectral method to solve the reactive Euler and Navier-Stokes equations submitted to a magnetic field is performed. The Euler and Navier-Stokes equations, coupled with the Maxwell equations, in conservative and finite volume contexts, employing structured spatial discretization, on a condition of thermochemical non-equilibrium, are studied. The spectral method presented in this work employs collocation points and variants of Chebyshev and Legendre interpolation functions are analyzed. The symmetrical algorithm of Maciel is used to perform the reentry flow numerical experiments, which give us an original contribution to the CFD community. The Mavriplis artificial dissipation model is applied. The "hot gas" hypersonic flows around a blunt body, around a double ellipse, and around a reentry capsule in two-dimensions are simulated. The Euler backward integration method is employed to march the scheme in time. The convergence process is accelerated to steady state condition through a spatially variable time step procedure, which has proved effective gains in terms of computational acceleration (see Maciel). The reactive simulations involve Earth atmosphere chemical model of five species and seventeen reactions, based on the Saxena and Nair model. N, O, N_2, O_2, and NO species are used to accomplish the numerical comparisons. The work of Gaitonde is the reference one to present the fluid dynamics and Maxwell equations of electromagnetism based on a conservative and finite volume formalisms. The results have indicated that the Chebyshev collocation point variants are more accurate in terms of stagnation pressure estimations in the viscous case. Errors inferior to 8.00% were found for this parameter in the viscous case, being 0.48% the best result. The Legendre collocation point variants are more accurate in terms of the lift coefficient estimations. Moreover, the Legendre collocation point variants are more computationally efficient and cheaper.

Keywords Spectral method; Hypersonic flow; Thermochemical non-equilibrium reentry flows; Reactive Euler and Navier-Stokes equations; Maxwell equations; High order accuracy.

1. Introduction

There are several approaches for computationally modeling fluid dynamics. These include finite difference, finite element, and spectral methods to name a few. Finite element and finite difference methods are frequently used and offer a wide range of well-known numerical schemes. These schemes can vary in terms of computational accuracy, but are typically of lower order of accuracy. If a more accurate solution is desired, it is common practice to refine the mesh either globally or in a region of interest. This can often be a complicated or time consuming process as global mesh refinement will greatly increase the computation time while local refinement requires an elaborated refinement operation, [1].

Alternatively, polynomial refinement has been used to improve the solution accuracy and has been shown to converge more quickly than mesh refinement in some cases [2-3]. For finite difference methods, polynomial refinement is performed by including neighboring node values in a higher order polynomial [4]. This can increase the complexity of the scheme especially near the boundaries where nodes do not exist to construct the

higher order polynomials. Finite element methods instead increase the number of unknown values within the cell itself to construct a higher order solution [5].

A scheme with a very high formal order of accuracy will not necessarily always produce the highest resolution. [6] demonstrated that a spectral-like scheme with a formal fourth-order accuracy produced a much more highly resolved solution than schemes with higher formal orders of accuracy when comparing modified wave numbers. Therefore, formal order of accuracy does not provide a comprehensive basis for selecting the best solution procedure. State-of-art methods such as spectral methods fall into this category.

Spectral methods are considered a class of solution techniques using sets of known functions to solve differential equations [7]. Such methods are generally considered high order and capable of obtaining solutions with a high resolution. Unlike finite-difference and finite-element methods, spectral methods utilize an expansion in terms of global, rather than local, basis functions to represent the solution of a differential equation. When properly applied, these techniques accurately resolve phenomena on the scale of the mesh spacing. The order of truncation error decay with mesh refinement is also higher than which can be achieved with finite-difference and finite-element methods. For problems with smooth solutions, it is possible to produce spectral method whose truncation error goes to zero as faster than any finite power of the mesh spacing (exponential convergence).

Spectral methods may be viewed as an extreme development of the class of discretization schemes known by the generic name of method of weighted residuals (MWR) [8]. The key elements of the MWR are the trial functions (also called the expansion or approximating functions) and the test functions (also known as weighted functions). The trial functions are used as the basis functions for a truncated series expansion of the solution that, when substituted into the differential equation, produces the residual. The test functions are used to enforce the minimization of the residual.

The choice of the trial functions is what distinguishes the spectral methods from the element and finite difference methods. The trial functions for spectral methods are infinitely differentiable global functions (Typically, they are tensor products of the eigenfunctions of singular Sturm-Liouville problems). In the case of finite element methods, the domain is divided into small elements and a trial function is specified in each element. The trial functions are thus local in character and well suited for handling complex geometries. The finite difference trial functions are likewise local.

The choice of test function distinguishes between Galerkin and collocation approaches. In the Galerkin approach, the test functions are the same as the trial functions, whereas in the collocation approach the test functions are translated Dirac delta functions. In other words, the Galerkin approach is equivalent to a least-square approximation, whereas the collocation approach requires the differential equations to be solved exactly at the collocation points.

The collocation approach is the simplest of the MWR and appears to have been first used by [9] in his study of electronic energy bands in metals. A few years later, [10] applied this method to the problem of torsion in square prism. [11] developed it as a general method for solving ordinary differential equations. They used a variety of trials functions and an arbitrary distribution of collocation points. The work of [12] established for the first time that a proper choice of the trial functions and the distribution of collocation points are crucial to the accuracy of the solution. Perhaps he should be credited with laying down the foundation of the orthogonal collocation method.

Spectral methods have been used on one-dimensional, compressible flow problems with piecewise linear solutions by [13-14]. These reports demonstrated that spectral methods, when combined with appropriate filtering techniques, can capture one-dimensional shock waves in otherwise featureless flows. A different sort of demonstration was provided by [15]. They exhibited spectral solutions of compressible flows with nontrivial structures in the smooth regions.

Renewed interest in the area of hypersonic flight has brought Computational Fluid Dynamics (CFD) to the forefront of fluid flow research [16]. Many years have seen a quantum leap in advancements made in the areas of computer systems and software which utilize them for problem solving. Sophisticated and accurate numerical algorithms are devised routinely that are capable of handling complex computational problems. Experimental test facilities capable of addressing complicated high-speed flow problems are still scarce because they are too

expensive to build and sophisticated measurements techniques appropriate for such problems, such as the non-intrusive laser, are still in the development stage. As a result, CFD has become a vital tool in the flow problem solution.

In chemical non-equilibrium flows the mass conservation equation is applied to each of the constituent species in the gas mixture. Therefore, the overall mass conservation equation is replaced by as many species conservation equations as the number of chemical species considered. The assumption of thermal non-equilibrium introduces additional energy conservation equations – one for every additional energy mode. Thus, the number of governing equations for non-equilibrium flow is much bigger compared to those for perfect gas flow. A complete set of governing equations for non-equilibrium flow may be found in [17-18].

The problems of chemical non-equilibrium in the shock layers over vehicles flying at high speeds and high altitudes in the Earth's atmosphere have been discussed by several investigators [19-22]. Most of the existing computer codes for calculating the non-equilibrium reacting flow use the one-temperature model, which assumes that all of the internal energy modes of the gaseous species are in equilibrium with the translational mode [21-22]. It has been pointed out that such a one-temperature description of the flow leads to a substantial overestimation of the rate of equilibrium because of the elevated vibrational temperature [20]. A three-temperature chemical-kinetic model has been proposed by [23] to describe the relaxation phenomena correctly in such a flight regime. However, the model is quite complex and requires many chemical rate parameters which are not yet known. As a compromise between the three-temperature and the conventional one-temperature model, a two-temperature chemical-kinetic model has been developed [24-25], which is designated herein as the TTv model. The TTv model uses one temperature T to characterize both the translational energy of the atoms and molecules and the rotational energy of the molecules, and another temperature Tv to characterize the vibrational energy of the molecules, translational energy of the electrons, and electronic excitation energy of atoms and molecules. The model has been applied to compute the thermodynamic properties behind a normal shock wave in a flow through a constant-area duct [24-25]. Radiation emission from the non-equilibrium flow has been calculated using the Non-equilibrium Air Radiation (NEQAIR) program [26-27]. The flow and the radiation computations have been packaged into a single computer program, the Shock-Tube Radiation Program (STRAP) [25].

The effects associated with the interaction of magnetic forces with conducting fluid flows have been profitably employed in several applications related to nuclear and other [28] technologies and are known to be essential in the explanation of astrophysical phenomena. In recent years, however, the study of these interactions has received fresh impetus in the effort to solve the problems of high drag and thermal loads encountered in hypersonic flight. The knowledge that electrical and magnetic forces can have profound influence on hypersonic flow fields is not new [29-30] – note increased shock-standoff and reduced heat transfer rates in hypersonic flows past blunt bodies under the application of appropriate magnetic fields. The recent interest stems, however, from new revelations of a Russian concept vehicle, known as AJAX [31], which made extensive reference to technologies requiring tight coupling between electromagnetic and fluid dynamic phenomena. A magnetogasdynamics (MGD) generator was proposed [32] to extract energy from the incoming air while simultaneously providing more benign flow to combustion components downstream. The extracted energy could then be employed to increase thrust by MGD pumping of the flow exiting the nozzle or to assist in the generation of a plasma for injection of the body. This latter technique is known to not only reduced drag on the body but also to provide thermal protection [33].

In addition to daunting engineering challenges, some of the phenomena supporting the feasibility of an AJAX type vehicle are fraught with controversy (see, for example, [34]). Resolution of these issues will require extensive experimentation as well as simulation. The latter approach requires integration of several disciplines, including fluid dynamics, electromagnetics, chemical kinetics, and molecular physics amongst others. This paper describes a recent effort to integrate the first three of these, within the assumptions that characterize ideal and non-ideal magnetogasdynamics.

In the present work, a study involving a spectral method to solve the reactive Euler and Navier-Stokes equations submitted to a magnetic field is performed. The Euler and Navier-Stokes equations, coupled with the Maxwell equations, in conservative and finite volume contexts, employing structured spatial discretization, on a condition

of thermochemical non-equilibrium, are studied. The spectral method presented in this work employs collocation points and variants of Chebyshev and Legendre interpolation functions are analyzed. The symmetrical algorithm of [35] is used to perform the reentry flow numerical experiments, which give us an original contribution to the CFD community. The [36] artificial dissipation model is applied. The "hot gas" hypersonic flows around a blunt body, around a double ellipse, and around a reentry capsule in two-dimensions are simulated. The Euler backward integration method is employed to march the scheme in time. The convergence process is accelerated to steady state condition through a spatially variable time step procedure, which has proved effective gains in terms of computational acceleration [37-38]. The reactive simulations involve Earth atmosphere chemical model of five species and seventeen reactions, based on the [39] model. N, O, N_2, O_2, and NO species are used to accomplish the numerical comparisons. The work of [40] is the reference one to present the fluid dynamics and Maxwell equations of electromagnetism based on a conservative and finite volume formalisms. The results have indicated that the Chebyshev collocation point variants are more accurate in terms of stagnation pressure estimations in the viscous case. Errors inferior to 8.00% were found for this parameter in the viscous case, being 0.48% the best result. The Legendre collocation point variants are more accurate in terms of the lift coefficient estimations. Moreover, the Legendre collocation point variants are more computationally efficient and cheaper.

2. Spectral Method

Two classes of techniques for spectral discretization are referred to as tau and collocation methods [41]. The latter technique is used here. In this scheme, the approximation series is determined by satisfying the differential equation exactly at a set of distinct collocation points. The locations of these points in the domain are linked to the choice of basis function. In this study, arbitrary collocation points are implemented. The collocation method is used here since enforcement of boundary conditions and evaluations of nonlinear terms are straightforward. Additionally, some accuracy advantage is seen in the collocation method over the tau method for a number of problems [41]. The series expansion for a function Q(x) may be represented as

$$Q_N(x) = \sum_{n=0}^{N} \hat{Q}_n B_n(x), \tag{1}$$

Where $B_n(x)$ are the basis functions and N is the total number of nodes employed in the interpolation process (It is also the order of accuracy of the spectral method). The coefficients $\hat{Q}_n$ are often termed the spectrum of $Q_N(x)$. One common technique used to evaluate the spectrum is to consider Eq. (1) as an interpolation series representing Q(x). The interpolation "nodes" of such series are the collocation points of the method. For a scheme based on Chebyshev collocation, the basis functions are:

$$B_n(x) = T_n(x) = 2xP_{n-1}(x) - P_{n-2}(x), \qquad n \geq 2, \tag{2}$$

with: $P_0(x) = 1$ and $P_1(x) = x$. The Chebyshev-Gauss-Lobatto standard collocation points are

$$x_l = \cos\left(\frac{\pi l}{N}\right), \qquad l = 0, 1, \ldots, N. \tag{3}$$

The Chebyshev collocation points result from a simple change of variables, which relates the Chebyshev interpolation series to a Fourier cosine series [41]. To evaluate the $\hat{Q}_n$, the inverse relation is required. This is

$$\hat{Q}_n = \hat{c}_n \sum_{l=0}^{N} w_l B_n(x_l) Q_{i,j}, \qquad n = 0, 1, \ldots, N, \tag{4}$$

withw_l being a normalized weighting function and $\hat{c}_n$ a constant. These variables assume the following expressions to a Chebyshev-Gauss-Lobatto interpolation:

$$\hat{c}_n = \frac{2}{N\bar{c}_n}, \text{ where: } \bar{c}_n = \begin{cases} 2, & n = 0 \text{ or } N \\ 1, & 1 < n < N-1 \end{cases}; \text{ and } \quad w_l = \frac{1}{\bar{c}_l}. \tag{5}$$

Legendre collocation is based on using Legendre polynomials as the basis function in Eq. (1), e.g.,

$$B_n(x) = \left[(2n-1)xP_{n-1}(x) - (n-1)P_{n-2}(x)\right]/n, \qquad n \geq 2, \tag{6}$$

where: $P_0(x) = 1$ and $P_1(x) = x$. Interpolation via Legendre series cannot easily be related to trigonometric interpolation, so there is no simple expression to evaluate the $\hat{Q}_n$ coefficients. Appeal must be made to the theory of numerical quadrature to form an approximation to the integrals which result from analytic Legendre interpolation [42]. Considering Eq. (4), the normalized weights and constant of the Legendre-Gauss-Lobatto collocation points are

$$w_l = \frac{1}{N(N+1)B_N^2(x_l)} \quad \text{and} \quad \hat{c}_n = \begin{cases} 2n+1, & n = 0,1,\ldots,N-1 \\ N, & n = N \end{cases}. \tag{7}$$

In this work, it was assumed that the Legendre-Gauss-Lobatto collocation points are the same as the Chebyshev-Gauss-Lobatto ones. It was also adopted the following collocation points and normalized weight for the Chebyshev-Gauss-Radau interpolation, based on the work of [43]:

$$x_l = \cos\left(\frac{2\pi l}{2N+1}\right), \tag{8}$$

$$w_l = \begin{cases} \dfrac{N}{2N+1}, & l = 0 \\ \dfrac{N}{N+1}, & \text{elsewhere} \end{cases}. \tag{9}$$

For the Legendre-Gauss-Radau interpolation, also based in [43], the collocation points are defined by Eq. (8) and the normalized weights are described by:

$$w_l = \begin{cases} \dfrac{1}{(N+1)^2}, & l = 0 \\ \dfrac{1}{2(N+1)^2} \times \dfrac{1-x_l}{B_N(x_l)}, & \text{elsewhere} \end{cases}. \tag{10}$$

The same calculation to the vector of conserved variables Q is applied to the vector of flux C, to be defined in section 4.

Hence, we have two collocation point options and two normalized weight functions to be considered by the Chebyshev and the Legendre methods, namely: Chebyshev-Gauss-Radau, Chebyshev-Gauss-Lobatto, Legendre-Gauss-Radau and Legendre-Gauss-Lobatto.

3. Reactive Navier-Stokes EquationsCoupled with Maxwell Equations in 2D

As the Navier-Stokes equations tend to the Euler equations when high Reynolds number are employed, only the former equations are presented coupled with the Maxwell equations. The reactive Navier-Stokes equations and the Maxwell equations in thermochemical non-equilibrium, where the rotational and vibrational contributions are considered,were implemented on conservative and finite volume contexts, in the two-dimensional space. In this case, these equations in integral and conservative forms can be expressed by:

$$\frac{\partial}{\partial t}\int_V Q dV + \int_S \vec{F} \bullet \vec{n} dS = \int_V S_{CV} dV, \text{ with: } \vec{F} = (E_e - E_v)\vec{i} + (F_e - F_v)\vec{j}, \tag{11}$$

where: Q is the vector of conserved variables, V is the volume of a computational cell, $\vec{F}$ is the complete flux vector, $\vec{n}$ is the unity vector normal to the flux face, S is the flux area, S_{CV} is the chemical and vibrational source term, E_e and F_e are the convective flux vectors or the Euler flux vectors in the x and y directions, respectively, and E_v and F_v are the viscous flux vectors in the x and y directions, respectively. The $\vec{i}$ and $\vec{j}$ unity vectors define the Cartesian coordinate system. Eleven (11) conservation equations are solved: one of general mass conservation, two of linear momentum conservation, one of total energy, four of species mass conservation, one of the vibrational internal energy of the molecules, and two of the Maxwell equations. Therefore, one of the species is absent of the iterative process. The CFD literature recommends that the species

of biggest mass fraction of the gaseous mixture should be omitted, aiming to result in a minor numerical accumulation error. To the present study, in which is chosen a chemical model to the air composed of five (5) chemical species (N, O, N_2, O_2, and NO) and seventeen chemical reactions to the [39] model, this species can be the N_2 or the O_2. To this work, the N_2 was chosen. The vectors Q, E_e, F_e, E_v, F_v, and S_{CV} can, hence, be defined as follows:

$$Q=\begin{Bmatrix}\rho\\ \rho u\\ \rho v\\ \rho Z\\ \rho_1\\ \rho_2\\ \rho_4\\ \rho_5\\ \rho e_V\\ B_x\\ B_y\end{Bmatrix},\ E_e=\begin{Bmatrix}\rho u\\ \rho u^2+P-R_b\,B_x^2/\mu_M\\ \rho uv-R_b B_x\,B_y/\mu_M\\ (\rho Z+P)u-R_b\left(\vec{V}\bullet\vec{B}/\mu_M\right)B_x\\ \rho_1 u\\ \rho_2 u\\ \rho_4 u\\ \rho_5 u\\ \rho e_V u\\ 0\\ uB_y-vB_x\end{Bmatrix},F_e=\begin{Bmatrix}\rho v\\ \rho uv-R_b\,B_xB_y/\mu_M\\ \rho v^2+P-R_b\,B_y^2/\mu_M\\ (\rho Z+P)v-R_b\left(\vec{V}\bullet\vec{B}/\mu_M\right)B_y\\ \rho_1 v\\ \rho_2 v\\ \rho_4 v\\ \rho_5 v\\ \rho e_V v\\ vB_x-uB_y\\ 0\end{Bmatrix};\qquad(12)$$

$$E_v=\begin{Bmatrix}0\\ \tau_{xx}/Re\\ \tau_{xy}/Re\\ (f_x-\phi_x)/Re-q_{J,x}/Re_\sigma\\ -\rho_1 v_{1x}/Re\\ -\rho_2 v_{2x}/Re\\ -\rho_4 v_{4x}/Re\\ -\rho_5 v_{5x}/Re\\ (q_{v,x}-\phi_{v,x})/Re\\ 0\\ \dfrac{1}{Re_\sigma}\dfrac{1}{\sigma}\left[\dfrac{\partial}{\partial x}\left(\dfrac{B_y}{\mu_M}\right)-\dfrac{\partial}{\partial y}\left(\dfrac{B_x}{\mu_M}\right)\right]\end{Bmatrix},F_v=\begin{Bmatrix}0\\ \tau_{xy}/Re\\ \tau_{yy}/Re\\ (f_y-\phi_y)/Re-q_{J,y}/Re_\sigma\\ -\rho_1 v_{1y}/Re\\ -\rho_2 v_{2y}/Re\\ -\rho_4 v_{4y}/Re\\ -\rho_5 v_{5y}/Re\\ (q_{v,y}-\phi_{v,y})/Re\\ \dfrac{1}{Re_\sigma}\dfrac{1}{\sigma}\left[\dfrac{\partial}{\partial y}\left(\dfrac{B_x}{\mu_M}\right)-\dfrac{\partial}{\partial x}\left(\dfrac{B_y}{\mu_M}\right)\right]\\ 0\end{Bmatrix};\qquad(13)$$

$$S_{CV}=\left\{0\quad 0\quad 0\quad 0\quad \dot{\omega}_1\quad \dot{\omega}_2\quad \dot{\omega}_4\quad \dot{\omega}_5\quad \sum_{s=mol}\rho_s\left(e^*_{v,s}-e_{v,s}\right)/\tau_s+\sum_{s=mol}\dot{\omega}_s e_{v,s}\quad 0\quad 0\right\}^T;\qquad(14)$$

in which: ρ is the mixture density; u and v are Cartesian components of the velocity vector in the x and y directions, respectively; $\vec{V}$ is the complete flow velocity vector; P is the pressure term considering the magnetic effect; Z is the fluid total energy considering the contribution of the magnetic field; ρ_1, ρ_2, ρ_4, and ρ_5 are densities of the N, O, O_2, and NO, respectively; B_x and B_y are Cartesian components of the magnetic field vector in the x and y directions, respectively; $\vec{B}$ is the complete magnetic field vector; R_b is the magnetic force number or the pressure number; μ_M is the mean magnetic permeability, with the value $4\pi x10^{-7}$T.m/A to the atmospheric air; e_V is the sum of the vibrational energy of the molecules; the τ's are the components of the Newtonian viscous stress tensor; f_x and f_y are viscous work and Fourier heat flux functions; $\rho_s v_{sx}$ and $\rho_s v_{sy}$ represent the species diffusion flux, defined by the Fick law; ϕ_x and ϕ_y are the terms of mixture diffusion; $\phi_{v,x}$

and $\phi_{v,y}$ are the terms of molecular diffusion calculated at the vibrational temperature; $\dot{\omega}_s$ is the chemical source term of each species equation, defined by the law of mass action; e_v^* is the molecular-vibrational-internal energy calculated with the translational/rotational temperature; τ_s is the translational-vibrational characteristic relaxation time of each molecule; $q_{v,x}$ and $q_{v,y}$ are the vibrational Fourier heat flux components in the x and y directions, respectively; Re is the laminar Reynolds number; $q_{J,x}$ and $q_{J,y}$ are the components of the Joule heat flux vector in the x and y directions, respectively; Re_σ is the magnetic Reynolds number and σ is the electrical conductivity.

The viscous stresses, in N/m^2, are determined, according to a Newtonian fluid model, by:

$$\tau_{xx} = \left[2\mu_m\, \partial u/\partial x - 2/3\mu_m\left(\partial u/\partial x + \partial v/\partial y\right)\right];$$
$$\tau_{xy} = \mu_m\left(\partial u/\partial y + \partial v/\partial x\right); \quad (15)$$
$$\tau_{yy} = \left[2\mu_m\, \partial v/\partial y - 2/3\mu_m\left(\partial u/\partial x + \partial v/\partial y\right)\right],$$

where μ_m is the molecular viscosity. Expressions to f_x and f_y are given below:

$$f_x = \tau_{xx}u + \tau_{xy}v + q_x + q_{v,x}; \quad (16)$$

$$f_y = \tau_{xy}u + \tau_{yy}v + q_y + q_{v,y}, \quad (17)$$

Where q_x and q_y are the Fourier heat flux components and are given by:

$$q_x = k\frac{\partial T}{\partial x} \text{ and } q_y = k\frac{\partial T}{\partial y}. \quad (18)$$

where: k is the thermal conductivity due to translation and rotation. The $q_{v,x}$ and $q_{v,y}$ are the vibrational heat flux components and are given by:

$$q_{v,x} = k_V\, \partial T_V/\partial x \text{ and } q_{v,y} = k_V\, \partial T_V/\partial y, \quad (19)$$

with k_V being the vibrational thermal conductivity and T_V is the vibrational temperature, what characterizes this model as of two temperatures: translational/rotational and vibrational. The terms of species diffusion, defined by the Fick law, to a condition of thermal non-equilibrium, are determined by [44]:

$$\rho_s v_{sx} = -\rho D_s \frac{\partial Y_{MF,s}}{\partial x} \text{ and } \rho_s v_{sy} = -\rho D_s \frac{\partial Y_{MF,s}}{\partial y}, \quad (20)$$

with "s" referent to a given species, $Y_{MF,s}$ being the molar fraction of the species, defined as:

$$Y_{MF,s} = \frac{\rho_s/M_s}{\sum_{k=1}^{ns}\rho_k/M_k} \quad (21)$$

and D_s is the species-effective-diffusion coefficient. "ns" is the number of species. The diffusion terms ϕ_x and ϕ_y which appear in the energy equation are defined by ([39]):

$$\phi_x = \sum_{s=1}^{ns}\rho_s v_{sx} h_s \text{ and } \phi_y = \sum_{s=1}^{ns}\rho_s v_{sy} h_s, \quad (22)$$

being h_s the specific enthalpy (sensible) of the chemical species "s". The molecular diffusion terms calculated at the vibrational temperature, $\phi_{v,x}$ and $\phi_{v,y}$, which appear in the vibrational-internal-energy equation are defined by [44]:

$$\phi_{v,x} = \sum_{s=mol}\rho_s v_{sx} h_{v,s} \text{ and } \phi_{v,y} = \sum_{s=mol}\rho_s v_{sy} h_{v,s}, \quad (23)$$

with $h_{v,s}$ being the specific enthalpy (sensible) of the chemical species "s" calculated at the vibrational temperature T_V. The sum of Eq. (14), as also those present in Eq. (23), considers only the molecules of the system, namely: N_2, O_2, and NO. The laminar Reynolds number is estimated by:

$$\mathrm{Re} = \frac{\rho_{char} V_{initial} L_{char}}{\mu_{m,char}}, \tag{24}$$

with "char" representing characteristic or freestream properties, ρ_{char} is the characteristic density, $V_{initial}$ is the flow initial velocity, L_{char} is a characteristic configuration length, and $\mu_{m,char}$ is a characteristic molecular viscosity. For details of the chemical model, the calculation of thermodynamic and transport properties see [45-46]. The Z total energy is defined as:

$$Z = c_{v,mix}\left(T - T_{REF}\right) + \Delta h^{0}_{f,mix} + e_V + 0.5\left(u^2 + v^2\right) + R_b \frac{B^2}{2\rho\mu_M}, \tag{25}$$

with: T_{REF} is the reference temperature, and $\Delta h^{0}_{f,mix}$ is the mixture formation enthalpy. The pressure term is given by:

$$P = p + R_b \frac{B_x^2 + B_y^2}{2\mu_M} = p + R_b \frac{B^2}{2\mu_M}, \tag{26}$$

with p the fluid static pressure. The magnetic force number or pressure number is determined by:

$$R_b = \frac{B^2_{initial}}{\rho_{char} V^2_{initial} \mu_{M,char}} = \frac{B^2_{x,initial} + B^2_{y,initial}}{\rho_{char}\left(u^2_{initial} + v^2_{initial}\right)\mu_{M,char}}, \tag{27}$$

The magnetic Reynolds number is calculated by:

$$\mathrm{Re}_\sigma = L_{char} V_{initial} \mu_{M,char} \sigma_{char}. \tag{28}$$

The components of the Joule heat flux vector, which characterizes the non-ideal formulation, are determined by:

$$q_{J,x} = -R_b \left\{ \frac{B_y}{\mu_M \sigma} \left[\frac{\partial}{\partial x}\left(\frac{B_y}{\mu_M}\right) - \frac{\partial}{\partial y}\left(\frac{B_x}{\mu_M}\right) \right] \right\} \text{ and } q_{J,y} = -R_b \left\{ \frac{B_x}{\mu_M \sigma} \left[\frac{\partial}{\partial y}\left(\frac{B_x}{\mu_M}\right) - \frac{\partial}{\partial x}\left(\frac{B_y}{\mu_M}\right) \right] \right\}. \tag{29}$$

4. Numerical Scheme

Maciel centered scheme is obtained by arithmetical average between the flux at the left and right states of the interface. Considering the two-dimensional and structured case, the algorithm is divided in three parts, as recommended by [47], each one corresponding to a characteristic flux. The first part takes into account the dynamic part, which considers the Navier-Stokes equations plus the Maxwell equations, the second one takes into account the chemical part, and the third part takes into account the vibrational part. Hence, the discrete-dynamic-convective flux, which solves the dynamic part, is given by:

$$R^{Dyn}_{i+1/2,j} = \frac{1}{2}\left[\begin{pmatrix} \rho u \\ \rho u^2 + P - R_b B_x^2/\mu_M \\ \rho uv - R_b B_x B_y/\mu_M \\ (\rho Z + P)u - R_b\left(\vec{V}\bullet\vec{B}/\mu_M\right)B_x \\ 0 \\ uB_y - vB_x \end{pmatrix}_L + \begin{pmatrix} \rho u \\ \rho u^2 + P - R_b B_x^2/\mu_M \\ \rho uv - R_b B_x B_y/\mu_M \\ (\rho Z + P)u - R_b\left(\vec{V}\bullet\vec{B}/\mu_M\right)B_x \\ 0 \\ uB_y - vB_x \end{pmatrix}_R \right] S_x +$$

$$+ \frac{1}{2}\left[\begin{pmatrix} \rho v \\ \rho uv - R_b B_x B_y/\mu_M \\ \rho v^2 + P - R_b B_y^2/\mu_M \\ (\rho Z + P)v - R_b\left(\vec{V}\bullet\vec{B}/\mu_M\right)B_y \\ vB_x - uB_y \\ 0 \end{pmatrix}_L + \begin{pmatrix} \rho v \\ \rho uv - R_b B_x B_y/\mu_M \\ \rho v^2 + P - R_b B_y^2/\mu_M \\ (\rho Z + P)v - R_b\left(\vec{V}\bullet\vec{B}/\mu_M\right)B_y \\ vB_x - uB_y \\ 0 \end{pmatrix}_R \right] S_y; \tag{30}$$

the discrete-chemical-convective flux is defined by:

$$R_{i+1/2,j}^{Chem}=\frac{1}{2}\left[\begin{pmatrix}\rho_1 u\\ \rho_2 u\\ \rho_4 u\\ \rho_5 u\end{pmatrix}_L+\begin{pmatrix}\rho_1 u\\ \rho_2 u\\ \rho_4 u\\ \rho_5 u\end{pmatrix}_R\right]S_x+\frac{1}{2}\left[\begin{pmatrix}\rho_1 v\\ \rho_2 v\\ \rho_4 v\\ \rho_5 v\end{pmatrix}_L+\begin{pmatrix}\rho_1 v\\ \rho_2 v\\ \rho_4 v\\ \rho_5 v\end{pmatrix}_R\right]S_y; \tag{31}$$

and the discrete-vibrational-convective flux is determined by:

$$R_{i+1/2,j}^{Vib}=\frac{1}{2}\left[(\rho e_v u)_L+(\rho e_v u)_R\right]S_x+\frac{1}{2}\left[(\rho e_v v)_L+(\rho e_v v)_R\right]S_y. \tag{32}$$

The viscous formulation follows that of [48], which adopts the Green theorem to calculate primitive variable gradients. The viscous gradients at the interfaces are also obtained by arithmetical average between cell (i,j) and its neighbors. As was done with the convective terms, there is a need to separate the viscous flux in three parts: dynamic viscous flux, chemical viscous flux and vibrational viscous flux. The dynamic part corresponds to:

$$R_{i+1/2,j}^{Dyn}=\frac{1}{2}\left[\begin{pmatrix}0\\ \tau_{xx}/Re\\ \tau_{xy}/Re\\ (f_x-\phi_x)/Re-q_{J,x}/Re_\sigma\\ 0\\ \frac{1}{Re_\sigma}\frac{1}{\sigma}\left[\frac{\partial}{\partial x}\left(\frac{B_y}{\mu_M}\right)-\frac{\partial}{\partial y}\left(\frac{B_x}{\mu_M}\right)\right]\end{pmatrix}_L+\begin{pmatrix}0\\ \tau_{xx}/Re\\ \tau_{xy}/Re\\ (f_x-\phi_x)/Re-q_{J,x}/Re_\sigma\\ 0\\ \frac{1}{Re_\sigma}\frac{1}{\sigma}\left[\frac{\partial}{\partial x}\left(\frac{B_y}{\mu_M}\right)-\frac{\partial}{\partial y}\left(\frac{B_x}{\mu_M}\right)\right]\end{pmatrix}_R\right]S_x+$$

$$\frac{1}{2}\left[\begin{pmatrix}0\\ \tau_{xy}/Re\\ \tau_{yy}/Re\\ (f_y-\phi_y)/Re-q_{J,y}/Re_\sigma\\ \frac{1}{Re_\sigma}\frac{1}{\sigma}\left[\frac{\partial}{\partial y}\left(\frac{B_x}{\mu_M}\right)-\frac{\partial}{\partial x}\left(\frac{B_y}{\mu_M}\right)\right]\\ 0\end{pmatrix}_L+\begin{pmatrix}0\\ \tau_{xy}/Re\\ \tau_{yy}/Re\\ (f_y-\phi_y)/Re-q_{J,y}/Re_\sigma\\ \frac{1}{Re_\sigma}\frac{1}{\sigma}\left[\frac{\partial}{\partial y}\left(\frac{B_x}{\mu_M}\right)-\frac{\partial}{\partial x}\left(\frac{B_y}{\mu_M}\right)\right]\\ 0\end{pmatrix}_R\right]S_y; \tag{33}$$

To the chemical part one has:

$$R_{i+1/2,j}^{Chem}=\frac{1}{2}\left[\begin{pmatrix}-\rho_1 v_{1x}/Re\\ -\rho_2 v_{2x}/Re\\ -\rho_4 v_{4x}/Re\\ -\rho_5 v_{5x}/Re\end{pmatrix}_L+\begin{pmatrix}-\rho_1 v_{1x}/Re\\ -\rho_2 v_{2x}/Re\\ -\rho_4 v_{4x}/Re\\ -\rho_5 v_{5x}/Re\end{pmatrix}_R\right]S_x+\frac{1}{2}\left[\begin{pmatrix}-\rho_1 v_{1y}/Re\\ -\rho_2 v_{2y}/Re\\ -\rho_4 v_{4y}/Re\\ -\rho_5 v_{5y}/Re\end{pmatrix}_L+\begin{pmatrix}-\rho_1 v_{1y}/Re\\ -\rho_2 v_{2y}/Re\\ -\rho_4 v_{4y}/Re\\ -\rho_5 v_{5y}/Re\end{pmatrix}_R\right]S_y; \tag{34}$$

Finally, to the vibrational part:

$$R_{i+1/2,j}^{Vib}=\frac{1}{2}\left[\left(\frac{q_{v,x}-\phi_{v,x}}{Re}\right)_L+\left(\frac{q_{v,x}-\phi_{v,x}}{Re}\right)_R\right]S_x+\frac{1}{2}\left[\left(\frac{q_{v,y}-\phi_{v,y}}{Re}\right)_L+\left(\frac{q_{v,y}-\phi_{v,y}}{Re}\right)_R\right]S_y. \tag{35}$$

where $S_{i+1/2,j}=\begin{bmatrix}S_x & S_y\end{bmatrix}^t_{i+1/2,j}$ defines the normal area vector for the surface (i+½,j). The normal area components S_x and S_y to each flux interface are given in Tab. 1. Figure 1 exhibits the computational cell adopted for the simulations, as well its respective nodes and flux interfaces. The resultant ordinary differential equation system can be written as:

$$V_{i,j}\, dQ_{i,j}/dt = -\left(R_{i,j-1/2} + R_{i+1/2,j} + R_{i,j+1/2} + R_{i-1/2,j}\right) = -C_{i,j}, \quad (36)$$

where the cell volume is given by:

$$V_{i,j} = 0.5\left|\left(x_{i,j} - x_{i+1,j}\right)y_{i+1,j+1} + \left(x_{i+1,j} - x_{i+1,j+1}\right)y_{i,j} + \left(x_{i+1,j+1} - x_{i,j}\right)y_{i+1,j}\right| +$$
$$0.5\left|\left(x_{i,j} - x_{i+1,j+1}\right)y_{i,j+1} + \left(x_{i+1,j+1} - x_{i,j+1}\right)y_{i,j} + \left(x_{i,j+1} - x_{i,j}\right)y_{i+1,j+1}\right|. \quad (37)$$

This scheme is high order accurate due to the employed spectral method, but is symmetrical and needs an artificial dissipation operator, D, to guarantee stability in presence of shock waves and background stabilities. Considering this operator, Eq. (36) can be rewritten as:

$$dQ_{i,j}/dt = -\left(C_{i,j} - D_{i,j}\right)/V_{i,j}, \quad (38)$$

where D has the following structure:

$$D\left(Q_{i,j}\right) = d^{(2)}\left(Q_{i,j}\right) - d^{(4)}\left(Q_{i,j}\right), \quad (39)$$

with:

$$d^{(2)} = 0.5\varepsilon^{(2)}_{i,j-1/2}\left(A_{i,j} + A_{i,j-1}\right)\left(Q_{i,j-1} - Q_{i,j}\right) + 0.5\varepsilon^{(2)}_{i+1/2,j}\left(A_{i,j} + A_{i+1,j}\right)\left(Q_{i+1,j} - Q_{i,j}\right) +$$
$$0.5\varepsilon^{(2)}_{i,j+1/2}\left(A_{i,j} + A_{i,j+1}\right)\left(Q_{i,j+1} - Q_{i,j}\right) + 0.5\varepsilon^{(2)}_{i-1/2,j}\left(A_{i,j} + A_{i-1,j}\right)\left(Q_{i-1,j} - Q_{i,j}\right), \quad (40)$$

named the undivided Laplacian operator, responsible by the numerical stability in presence of shock waves; and

$$d^{(4)} = 0.5\varepsilon^{(4)}_{i,j-1/2}\left(A_{i,j} + A_{i,j-1}\right)\left(\nabla^2 Q_{i,j-1} - \nabla^2 Q_{i,j}\right) + 0.5\varepsilon^{(4)}_{i+1/2,j}\left(A_{i,j} + A_{i+1,j}\right)\left(\nabla^2 Q_{i+1,j} - \nabla^2 Q_{i,j}\right) +$$
$$0.5\varepsilon^{(4)}_{i,j+1/2}\left(A_{i,j} + A_{i,j+1}\right)\left(\nabla^2 Q_{i,j+1} - \nabla^2 Q_{i,j}\right) + 0.5\varepsilon^{(4)}_{i-1/2,j}\left(A_{i,j} + A_{i-1,j}\right)\left(\nabla^2 Q_{i-1,j} - \nabla^2 Q_{i,j}\right), \quad (41)$$

named the bi-harmonic operator, responsible by the background stability (odd-even instabilities, for instance). In this last term,

$$\nabla^2 Q_{i,j} = \left(Q_{i,j-1} - Q_{i,j}\right) + \left(Q_{i+1,j} - Q_{i,j}\right) + \left(Q_{i,j+1} - Q_{i,j}\right) + \left(Q_{i-1,j} - Q_{i,j}\right). \quad (42)$$

In the $d^{(4)}$ operator, $\nabla^2 Q_{i,j}$ is extrapolated from your neighbor cell every time that such one represent an especial boundary layer cell, recognized in the CFD literature as "ghost" cell. The ε terms are defined, for example, as:

$$\varepsilon^{(2)}_{i,j-1/2} = K^{(2)} MAX\left(\nu_{i,j}, \nu_{i,j-1}\right) \text{and } \varepsilon^{(4)}_{i,j-1/2} = MAX\left[0, \left(K^{(4)} - \varepsilon^{(2)}_{i,j-1/2}\right)\right], \quad (43)$$

in which:

$$\nu_{i,j} = \left(\left|p_{i,j-1} - p_{i,j}\right| + \left|p_{i+1,j} - p_{i,j}\right| + \left|p_{i,j+1} - p_{i,j}\right| + \left|p_{i-1,j} - p_{i,j}\right|\right)/\left(p_{i,j-1} + p_{i+1,j} + p_{i,j+1} + p_{i-1,j} + 4p_{i,j}\right) \quad (44)$$

represents a pressure sensor employed to identify regions of high gradients. Each time that a neighbor cell represent a ghost cell, it is assumed that, for instance, $\nu_{ghost} = \nu_{i,j}$. The $A_{i,j}$ terms define the particular artificial dissipation operator. In the present study, the $A_{i,j}$ terms represent the sum of the contributions of the maximum normal eigenvalue associated to the flux interface of the Euler equations, integrated along each cell face. This model is based on the work of [36].

$$A_{i,j} = \left|u_{int}S_x + v_{int}S_y\right|_{i,j-1/2} + a_{int}\left(S_x^2 + S_y^2\right)^{0.5}_{i,j-1/2}\Big| + \left|u_{int}S_x + v_{int}S_y\right|_{i+1/2,j} + a_{int}\left(S_x^2 + S_y^2\right)^{0.5}_{i+1/2,j}\Big| +$$
$$\left|u_{int}S_x + v_{int}S_y\right|_{i,j+1/2} + a_{int}\left(S_x^2 + S_y^2\right)^{0.5}_{i,j+1/2}\Big| + \left|u_{int}S_x + v_{int}S_y\right|_{i-1/2,j} + a_{int}\left(S_x^2 + S_y^2\right)^{0.5}_{i-1/2,j}\Big|, \quad (45)$$

where "a" represents the sound speed and the interface properties are evaluated by arithmetical average. The $K^{(2)}$ and $K^{(4)}$ constants have typical values of 1/4 and 3/256, respectively.

To march the scheme in time, the Euler backward method was implemented. This method is first-order accurate in time, to the three types of complete flux. To the dynamic part, this method can be represented in general form by:

$$Q_{i,j}^{(n+1)} = Q_{i,j}^{(n)} - \left(\Delta t_{i,j}/V_{i,j}\right)\times\left[C\left(Q_{i,j}^{(n)}\right) - D\left(Q_{i,j}^{(n)}\right)\right], \quad (46)$$

to the chemical part, it can be represented in general form by:

$$Q_{i,j}^{(n+1)} = Q_{i,j}^{(n)} - \Delta t_{i,j}\times\left\{\left[C\left(Q_{i,j}^{(n)}\right) - D\left(Q_{i,j}^{(n)}\right)\right]/V_{i,j} - S_C\left(Q_{i,j}^{(n)}\right)\right\}, \quad (47)$$

where the chemical source term S_C is calculated with the temperature T_{rrc} (reaction rate controlling temperature, see [45-46]). Finally, to the vibrational part:

$$Q_{i,j}^{(n+1)} = Q_{i,j}^{(n)} - \Delta t_{i,j}\times\left\{\left[C\left(Q_{i,j}^{(n)}\right) - D\left(Q_{i,j}^{(n)}\right)\right]/V_{i,j} - S_V\left(Q_{i,j}^{(n)}\right)\right\}, \quad (48)$$

in which:

$$S_V = \sum_{s=mol} q_{T-V,s} + \sum_{s=mol} S_{C,s} e_{v,s}\ , \quad (49)$$

where $q_{T\text{-}V}$ is the heat flux due to translational-vibrational relaxation, defined in [45-46].

5. Spatially Variable Time Step

The spatially variable time step has proved efficient gains in terms of convergence acceleration, as verified by [37-38]. Initially, the parameter σ is determined, where:

$$\sigma_s = \frac{c_s}{M_s} \text{ and } \sigma = \sum_{s=1}^{ns} \sigma_s\ , \quad (50)$$

with c_s being the mass fraction, and M_s the molecular weight. The total specific heat at constant volume due to translation is defined as:

$$c_{V,T} = \sum_{s=1}^{ns} \sigma_s c_{V,T,s}\ , \quad (51)$$

where, for each gas constituent of the five (5) species chemical model, the specific heat at constant volume, based on the kinetic theory of gases [49], is defined by

$$c_{V,T,N} = \frac{3}{2}R_N,\ c_{V,T,O} = \frac{3}{2}R_O,\ c_{V,T,N_2} = \frac{5}{2}R_{N_2},\ c_{V,T,O_2} = \frac{5}{2}R_{O_2}, \text{ and } c_{V,T,NO} = \frac{5}{2}R_{NO}, \quad (52)$$

being R_s the specific gas constant. The total pressure of the gaseous mixture is determined by Dalton law, which indicates that the total pressure of the gas is the sum of the partial pressure of each constituent gas, resulting in:

$$p_s = c_s \rho R_s T \text{ and } p = \sum_{s=1}^{ns} p_s\ . \quad (53)$$

The speed of sound to a reactive mixture can be determined by:

$$a = \sqrt{\frac{(1+\beta)p}{\rho}}\ , \quad (54)$$

where $\beta = \frac{R_{univ}\sigma}{c_{V,T}}$, with R_{univ} = 1.987 cal/(g-mol.K). Finally, the spatially variable time step is defined from the CFL (Courant-Friedrichs-Lewis) definition:

$$\Delta t_{i,j} = \frac{CFL\Delta s_{i,j}}{\sqrt{u_{i,j}^2 + v_{i,j}^2} + a_{i,j}}\ , \quad (55)$$

2here $\Delta s_{i,j}$ is the characteristic length of each cell (defined between the minimum cell side length and the minimum centroid distance between each cell and its neighbors).

6. Dimensionless Scales, Initial and Boundary Conditions

6.1. Dimensionless Scales

The dimensionless scales employed to the reactive equations consisted in: R_s is dimensionless by a_{char}, where

$a_{char} = \sqrt{\gamma p_{char}/\rho_{char}}$; c_v is dimensionless by a_{char}; h_s and Δh_s^0 are dimensionless by a_{char}^2; T and T_v, translational/rotational temperature and vibrational temperature, respectively, are dimensionless by a_{char}; ρ_s and ρ are dimensionless by ρ_{char}; u and v are dimensionless by a_{char}; μ is dimensionless by μ_{char}; D, diffusion coefficient, dimensionless by $a_{char}^2\, dt_{char}$, where dt_{char} is the minimum time step calculated in the computational domain at the first iteration; $\dot{\omega}$ is dimensionless by $(\rho_{char}/dt_{char})x10^{-3}$; e_v is dimensionless by a_{char}^2; p is dimensionless by $\rho_{char} a_{char}^2$; τ_s, relaxation time, is dimensionless by dt_{char}. To the Maxwell equations: the B_x and B_y Cartesian components of the magnetic field dimensionless by $B_{initial}$; the magnetic permeability of the mean is dimensionless by $\mu_{M,char}$; and the electric conductivity is dimensionless by σ_{char}. The characteristic physical properties are defined in [50].

6.2. Initial Condition

The initial conditions to the blunt body, to the double ellipse, and to the reentry capsule problems, for a five species chemical model, are presented in Tabs. 2-4. The Reynolds number is obtained from data of [50].

6.3. Boundary Conditions

The boundary conditions are basically of four types: solid wall, entrance, exit, and continuity. These conditions are implemented with the help of ghost cells.

Wall condition

In the inviscid case, this condition imposes the flow tangency at wall. This condition is satisfied considering the velocity component tangent to the wall relative to the ghost cell as equal to the respective component of the real neighbor cell. At the same time, the velocity component normal to the wall relative to the ghost cell is equaled to the negative of the corresponding component of the real neighbor cell. This procedure leads to a system of equations which results in:

$$u_g = \left(n_y^2 - n_x^2\right)u_r + \left(-2n_x n_y\right)v_r; \tag{56}$$

$$v_g = \left(-2n_x n_y\right)u_r + \left(n_x^2 - n_y^2\right)v_r, \tag{57}$$

where "g" indicates ghost cell properties and "r" indicates real cell properties. In the viscous case, the non-slip condition is enforced. Therefore, the tangent velocity component of the ghost volume at wall has the same magnitude as the respective velocity component of its real neighbor cell, but opposite signal. In the same way, the normal velocity component of the ghost volume at wall is equal in value, but opposite in signal, to the respective velocity component of its real neighbor cell. It results in:

$$u_g = -u_r \text{ and } v_g = -v_r. \tag{58}$$

The normal pressure gradient of the fluid at the wall is assumed to be equal to zero according to an inviscid formulation or a boundary-layer like condition. The same hypothesis is applied for the normal temperature gradient at the wall, assuming an adiabatic wall. From these considerations, density and translational/rotational temperature are extrapolated from the respective values of its real neighbor volume (zero order extrapolation). The total vibrational internal energy is also extrapolated.

With the mixture species mass fractions and with the values of the respective specific heats at constant volume, it is possible to obtain the mixture specific heat at constant volume. The mixture formation enthalpy is extrapolated from the real cell. The Cartesian components of the induced magnetic field at the wall to the ghost cells are fixed with their initial values. The magnetic permeability is considered constant with its initial value. The mixture total energy to the ghost cell is calculated by:

$$Z_g = c_{v,mixt,g}\left(T_{tr,g} - T_{REF}\right) + \Delta h^0_{mixt,g} + e_{v,g} + 0.5\left(u_g^2 + v_g^2\right) + R_b\left(B_{x,g}^2 + B_{y,g}^2\right)/\left(2\mu_{M,g}\rho_g\right), \tag{59}$$

To the species density, the non-catalytic condition is imposed, what corresponds to zero order extrapolation from the real cell.

Entrance condition

It is divided in two flow regimes:

(a) Subsonic flow: Five properties are specified and one extrapolated in the boundary conditions of the dynamic part of the algorithm. This approach is based on information propagation analysis along characteristic directions in the calculation domain ([51]). In other words, for subsonic flow, five characteristics propagate information point into the computational domain. Thus five flow properties must be fixed at the inlet plane. Just one characteristic line allows information to travel upstream. So, one flow variable must be extrapolated from the interior grid to the inlet boundary. The total energy was the extrapolated variable from the real neighbor volumes, for the studied problems. Density, velocity components, and the induced magnetic field components adopted values of initial flow. To the chemical part, four information propagate upstream because it is assumed that all four equations are conducted by the eigenvalue "(q_n-a)". In the subsonic flow, all eigenvalues are negative and the information should be extrapolated. In the same reasoning to the chemical boundary conditions, the vibrational-internal-energy equation is dictated by the "(q_n-a)" eigenvalue and, in the subsonic region, its value is negative. Hence, the vibrational internal energy should be extrapolated.

(b) Supersonic flow: In this case no information travels upstream; therefore all variables are fixed with their initial values.

Exit condition

It is also divided in two flow regimes:

(a) Subsonic flow: Five characteristics propagate information outward the computational domain. Hence, the associated variables should be extrapolated from interior information. The characteristic direction associated to the "(q_{normal}-a)" velocity should be specified because it points inward to the computational domain ([51]). In this case, the ghost volume total energy is specified from its initial value. Density, velocity components, and the induced magnetic field components are extrapolated. To the chemical part, the eigenvalue "(q_n-a)" is again negative and the characteristics are always flowing into the computational domain. Hence, the four chemical species under study should have their densities fixed by their initial values. In the same reasoning, the internal vibrational energy should have their value prescribed by its initial value due to the eigenvalue "(q_n-a)" be negative.

(b) Supersonic flow: All variables are extrapolated from interior grid cells, as no flow information can make its way upstream. In other words,nothing can be fixed.

Continuity condition

This condition imposes continuity of the flow at the trailing edge of the reentry capsule configuration. This is done considering the Kutta condition in this region. In terms of numerical implementation, it is obtained considering the vector of conserved variables above the wake as equal to the vector of conserved variables below the wake.

7. Physical Problems

Three physical problems were solved in this work, namely: blunt body, double ellipse, and reentry capsule. The first problem considers the geometry of a blunt body with 1.0 m of nose ratio and parallel rectilinear walls. The far field is located at 20.0 times the nose ratio in relation to the configuration nose. A mesh composed of 2,548 rectangular cells and 2,650 nodes was studied for the inviscid case, with an exponential stretching of 5.0% for the viscous case. This mesh is equivalent in finite differences to a one of 53x50 points. Figure 2 shows the detail of the geometry and Figs. 3 and 4 exhibit the inviscid and viscous meshes.

The double ellipse problem is the second under study. The mesh is composed of 4,116 rectangular cells and 4,250 nodes, with an exponential stretching of 5.0% for the viscous case, and far field located at 20.0 unities. This mesh is equivalent in finite differences to a one of 85x50 points. Figure 5 shows the double ellipse geometry and Figs. 6 and 7 exhibit the inviscid and viscous meshes.

The third problem is the geometry of the reentry capsule. Details of the configuration are presented in Fig. 8. The far field is located also at 20.0 unities. A mesh of 3,136 rectangular cells and 3,250 nodes was used for the

inviscid case, whereas with an exponential stretching of 5.0% was used for the viscous simulations. This mesh is equivalent in finite differences to a one of 65x50 points. Figures 9 and 10 show the inviscid and viscous meshes.

8. Results

Tests were performed in a Core i7 processor of 2.1GHz and 6.0Gbytes of RAM microcomputer, in a Windows 7.0 environment. Three (3) orders of reduction of the maximum residual in the field were considered to obtain a converged solution. The residual was defined as the value of the discretized conservation equation. In the dynamic part of the [35] scheme, such definition results in:

$$\text{Residual} = -\Delta t_{i,j} / V_{i,j} \times \left(C_{i,j} - D_{i,j}\right). \quad (60)$$

The attack angle was adopted equal to zero. In this work, the inviscid results were obtained for a 5^{th} order of accuracy of the spectral method, whereas the viscous solutions were obtained for an 8^{th} order of accuracy of the spectral method. The inviscid double ellipse problem did not generate converged results as also the viscous reentry capsule problem. For a matter of simplicity, the following abbreviations were used: [35] scheme = MAC, Chebyshev-Gauss-Radau = CGR, Chebyshev-Gauss-Lobatto = CGL, Legendre-Gauss-Radau = LGR, and Legendre-Gauss-Lobatto = LGL.

8.1. Blunt Body Problem

Inviscid case

Figures 11 to 14 exhibit the pressure, the translational/rotational temperature, the B_x component of the magnetic field, and the N_2 mass fraction contours obtained by the MAC scheme as using the CGR collocation points. The MAC algorithm captures accurately the shock wave. Good symmetry and homogenous properties are observed in these figures. No pre-shock oscillations are observed. The maximum temperature at the configuration nose is 11,459.90K.

Figures 15 to 18 show the pressure, the translational/rotational temperature, the B_x component of the magnetic field, and the N_2 mass fraction contours generated by the MAC scheme as using CGL collocation points. The maximum pressure is inferior to that observed in the CGR case. The B_x component of the magnetic field, the temperature and the N_2 mass fraction contours present good symmetry properties. The maximum temperature in the field reaches the value of 11,510.30K. The contours are free of oscillations.

Figures 19 to 22 present the pressure, the translational/rotational temperature, the B_x component of the magnetic field, and the N_2 mass fraction contours generated by the MAC scheme when using the LGR collocation points. The pressure peak is smaller than those obtained in the Chebyshev variants. No pressure oscillations are observed and good symmetry properties are verified in all figures. The maximum temperature peak in the field is 11,534.00K, and is superior than those obtained by the Chebyshev variants.

Figures 23 to 26 exhibit the pressure, the translational/rotational temperature, the B_x component of the magnetic field, and the N_2 mass fraction contours generated by the MAC scheme when using the LGL collocation points. The pressure peak in the field is still low. Good symmetry and homogeneous properties are observed and the shock wave is well captured. The temperature contours present also good symmetry properties, free of oscillations. The B_x component of the magnetic field presents good symmetry properties, and the N_2 suffers good dissociation. The maximum temperature in the field is 11,502.10K.

Viscous case

Figures 27 to 30 present the pressure, the translational/rotational temperature, the B_x component of the magnetic field, and the N_2 mass fraction contours generated by the MAC scheme as using CGR collocation points. The pressure peak is very close to the theoretical stagnation pressure value. Good symmetry properties are observed and no pre-shock oscillations are observed. The B_x component of the magnetic field presents good homogenous properties and good dissociation of N_2 is observed. The maximum temperature reaches the mark of 16,644.10K. Good symmetry properties are verified in the temperature field. Note that the correct transport of properties like viscosity and thermal conduction are qualitatively confirmed.

Figures 31 to 34 show the pressure, the translational/rotational temperature, the B_x component of the magnetic field, and the N_2 mass fraction contours generated by the MAC scheme when using CGL collocation points. Again the pressure peak is close to the theoretical value of stagnation pressure (see Table 5). The shock wave is

well captured by the scheme. The B_x component of the magnetic field is well captured and good dissociation of N_2 is observed, with some oscillations in the solution. Figure 32 shows the translational/rotational temperature contours and the good transport of viscosity and thermal conduction is noted in the MAC solution. The maximum temperature in the field is 18,139.60K.

Figures 35 to 38 exhibit the pressure, the translational/rotational temperature, the B_x component of the magnetic field, and the N_2 mass fraction contours generated by the MAC scheme as using the LGR collocation points. The pressure peak in the field is lower than those of the CGR and CGL variants. Good symmetry properties are observed in all figures, free of pre-shock oscillations. The maximum temperature in the field reaches the value of 19,810.90K. Good homogenous properties are observed in all figures.

Figures 39 to 42 present the pressure, the translational/rotational temperature, the B_x component of the magnetic field, and the N_2 mass fraction contours generated by the MAC scheme when using the LGL collocation points. The pressure peak is reduced in relation to the theoretical stagnation pressure value. All solutions present good symmetry and homogenous properties, free of oscillations. The shock wave is well captured and the transport of viscous properties is well highlighted in the MAC's temperature contours. The maximum temperature reaches the value of 19,791.10K. The Legendre solutions present in general higher values to the stagnation temperature than the Chebyshev solutions. It is clear that Chebyshev variants dominate the pressure field, whereas the Legendre variants dominate the temperature field.

8.2. Double Ellipse Problem

Viscous case

Figures 43 to 46 exhibit the pressure, the translational/rotational temperature, the B_x component of the magnetic field, and the N_2 mass fraction contours generated by the MAC scheme as using the CGR variant of the proposed spectral method. The pressure peak is close to the theoretical stagnation pressure, with an error of 5.03%. Good homogenous properties are observed in all solutions, with the N_2 contours presenting some oscillations. Figure 44 exhibits the thermal boundary layer captured by the numerical scheme. No temperature oscillations are observed in this figure. The maximum temperature field is calculated with the value of 15,887.90K.

Figures 47 to 50 show the pressure, the translational/rotational temperature, the B_x component of the magnetic field, and the N_2 mass fraction contours generated by the MAC scheme when using CGL collocation points. Again the pressure peak is close to the theoretical value of stagnation pressure (see Table 5). The shock wave is well captured by the scheme. The B_x component of the magnetic field is well captured and good dissociation of N_2 is observed, with some oscillations in the solution. The maximum temperature in the field is 16,483.50K.

Figures 51 to 54 exhibit the pressure, the translational/rotational temperature, the B_x component of the magnetic field, and the N_2 mass fraction contours generated by the MAC scheme as using the LGR collocation points. The pressure peak in the field is lower than those of the CGR and CGL variants, but still high. Good symmetry properties are observed in all figures, free of pre-shock oscillations. The maximum temperature in the field reaches the mark of 21,124.90K. Good homogenous properties are observed in all figures.

Figures 55 to 58 present the pressure, the translational/rotational temperature, the B_x component of the magnetic field, and the N_2 mass fraction contours generated by the MAC scheme when using the LGL collocation points. The pressure peak is reduced in relation to the theoretical stagnation pressure value, but superior to the LGR value. All solutions present good symmetry and homogenous properties, free of oscillations. The shock wave is well captured. The maximum temperature reaches the value of 21,162.70K.The Legendre solutions again present higher values to the stagnation temperature than the Chebyshev solutions, ratifying the behavior observed in the blunt body problem.

8.3. Reentry Capsule Problem

Inviscid case

Figures 59 to 62 present the pressure, the translational/rotational temperature, the B_x component of the magnetic field, and the N_2 mass fraction contours generated by the MAC scheme as using the CGR collocation points. Good symmetry and homogenous properties are verified in all contours. The stagnation pressure estimated by

the MAC scheme as using CGR collocation points is the best in comparison with the CGL, LGR, and LGL solutions, with an error of 3.72%.The Kutta condition was correctly implemented. Good dissociation of N_2 is verified. The shock wave is well captured by the MAC scheme. The maximum temperature in the field has the value of 9,400.85K

Figures 63 to 66 show the pressure, the translational/rotational temperature, the B_x component of the magnetic field, and the N_2 mass fraction contours generated by the MAC scheme when using the CGL collocation points. Good symmetry properties are observed in all solutions, free of pre-shock oscillations. Good dissociation of N_2 is observed. The maximum temperature peak has the value of 9,674.47K.

Figures 67 to 70 exhibit the pressure, the translational/rotational temperature, the B_x component of the magnetic field, and the N_2 mass fraction contours generated by the MAC scheme as using the LGR collocation points. The values of stagnation pressure obtained by the numerical scheme are inferior to the theoretical value. As mentioned before, it is clear that the Legendre variant behaves better for the temperature field and for the determination of the lift aerodynamic coefficient, as seen in Tabs. 8 and 9. Good symmetry properties are observed in all solutions and free of oscillations. The maximum temperature in the field has the value of 10,202.10K.

Figures 71 to 74 show the pressure, the translational/rotational temperature, the B_x component of the magnetic field, and the N_2 mass fraction contours generated by the MAC scheme as using the LGL collocation points. The normal shock wave ahead of the configuration nose is well captured. Moreover, the stagnation pressure value is under-predicted in relation to the theoretical value. Good symmetry and homogenous properties are verified in all the solutions. Good dissociation of N_2 is observed. The trailing edge flow is well captured by the numerical scheme, emphasizing the correct implementation of the Kutta condition. The maximum temperature in the field reaches the value of 10,254.30K.

8.4. Other Comparisons

Figure 75 shows the convergence histories of the MAC scheme for a 5^{th} order spectral method using LGR for collocation points and of the 2^{nd} order MAC scheme, to the blunt body inviscid case and Fig. 76 exhibits the convergence histories of the MAC scheme for a 8^{th} order spectral method using also LGR for collocation points and of the 2^{nd} order MAC scheme, also to the blunt body problem. The LGR collocation points were chosen because they provide the best convergence of the MAC scheme for the inviscid and viscous cases. The 2^{nd} order MAC scheme was implemented by the author and was used for numerical comparisons. To details of the implementation of the 2^{nd} order MAC scheme on a context of thermochemical non-equilibrium, the reader is encouraged to read [35]. As can be seen in Fig. 75, the spectral (LGR) method coupled with the MAC scheme was the most efficient converging in 1,147 iterations, with a maximum CFL of 0.10. The 2^{nd} order MAC solution was very inefficient compared with the spectral method. The maximum allowable CFL number employed in the 2^{nd} order MAC solution was 0.05. Figure 76 compares the 2^{nd} order MAC solution, and the spectral (LGR) method for the viscous case. In this case, the good convergence of the spectral (LGR) method was highlighted, converging in 1,569 iterations, whereas the 2^{nd} order MAC solution converged in more than 5,000 iterations, employing a CFL number of 0.05.

As conclusion, the correct implementation of the proposed spectral method leant to an efficient high order scheme, converging in less than 1,150 iterations in the inviscid case, for the blunt body problem, when programmed coupled with the MAC scheme. The LGR variant of the spectral method was the most efficient in the studies performed by the author and ratified the fast convergence as expected.

8.5. Quantitative Analysis

In order to perform a quantitative analysis, the present reactive results are compared to the perfect gas solutions. The stagnation pressures at the blunt body nose, at the double ellipse nose, and at the reentry capsule nose were evaluated assuming the perfect gas formulation. Such parameter calculated at this way is not the best comparison, but in the absence of practical reactive results, this constitutes the best available solution.

To calculate the stagnation pressure at the nose of these three configurations, [52] presents in its B Appendix values of the normal shock wave properties ahead of the configuration. The ratio pr_0/pr_∞ is estimated as function

of the normal Mach number and the stagnation pressure pr_0 can be determined from this parameter. Hence, Table 5 gives the theoretical stagnation pressure values obtained for the three configurations at the initial-normal-Mach number. The value of pr_∞ is determined by the following expression:

$$pr_\infty = \frac{pr_{initial}}{\rho_{char} \times a_{char}^2}, \tag{61}$$

where, for example, for the blunt body case, $pr_{initial}$ = 687N/m^2, ρ_{char} = 0.004kg/m^3 and a_{char} = 317.024m/s. Considering these values, one concludes that pr_∞ = 1.709 (non-dimensional). Using the ratio obtained from [52], the stagnation pressure ahead of the configuration nose is estimated as 170.87 unities. Tables 6 (inviscid case) and 7 (viscous case) compare values of the stagnation pressure obtained from the simulations with the theoretical values and show the percentage errors. As can be seen, the best results in the inviscid case are provided by the CGR collocation points, with an error of 39.58%, when coupled with the MAC scheme, for the blunt body problem; and again by CGR collocation points, with an error of 3.72%, when coupled with the MAC scheme, for the reentry capsule problem. For the viscous case, the CGR collocation points, with an error of 0.48%, coupled with the MAC scheme, for the blunt body problem, was the best; and with the CGR collocation points, with an error of 5.03%, coupled with the MAC scheme, for the double ellipse problem, was the best.

As the hypersonic flows around the blunt body, and reentry capsule configurations were simulated with a zero value to the attack angle, a zero lift coefficient, due to geometry symmetry, is the expected value for this aerodynamic coefficient. Tables 8 (inviscid) and 9 (viscous) present an analysis of the lift aerodynamic coefficient, based only on pressure contribution, in this study. As can be observed, the best value to the lift coefficient in the inviscid case is obtained by the LGL collocation points, coupled with the MAC scheme, for the blunt body problem; and again by the LGL collocation points, coupled with the MAC scheme, for the reentry capsule problem. In the viscous case, the best value to the lift coefficient is obtained by the CGL collocation points, coupled with the MAC scheme, for the blunt body problem.

8.6. Computational Performance

Tables 10 and 11 present the computational data of the MAC scheme for the blunt body, for the double ellipse, and for the reentry capsule problems in both inviscid and viscous cases. It shows the CFL number and the number of iterations to convergence for all studied cases in the current work. It can be verified that the best performance of the MAC scheme in the inviscid case occurred when using the LGR collocation points, employing a CFL of 0.10, and converging in 1,147 iterations, in the blunt body problem, whereas in the viscous case occurred when using the LGR collocation points, employing a CFL of 0.10, and converging in 1,569 iterations, also in the blunt body problem.

As final conclusion, it is possible to highlight that, for the blunt body problem, the MAC scheme in the viscous case using CGR collocation points had the best performance in estimating the stagnation pressure, and the lift aerodynamic coefficient was best estimated by the MAC scheme as using the CGL collocation points; for the double ellipse problem, the MAC scheme in the viscous case using CGR collocation points had the best performance in estimating the stagnation pressure; and finally, for the reentry capsule problem, the MAC scheme in the inviscid case using CGR collocation points had the best performance in estimating the stagnation pressure, and the lift aerodynamic coefficient was best estimated by the MAC scheme as using the LGL collocation points. Moreover, the best performance of the numerical schemes, for the 5th order of accuracy, was due to the MAC one, when using the LGR collocation points, employing a CFL of 0.10, and converging in 1,147 iterations, in the blunt body problem, whereas for the 8th order of accuracy, the best performance of the numerical scheme was due to the MAC one, when using the LGR collocation points, employing a CFL of 0.10, and converging in 1,569 iterations, also in the blunt body problem.

Finally, to close this work, the computational cost of the numerical schemes using the several types of collocation points is presented in Tab. 12. For the inviscid case, the cheapest combination was the MAC scheme using CGL collocation points with a cost of 0.00017704 sec/per-volume/per-iteration, whereas for the viscous case the cheapest was due to the MAC scheme coupled with the LGR collocation points with a cost of 0.00042148 sec/per-volume/per-iteration.

Table 1: Values of S_x and S_y

Surface	S_x	S_y
i,j-1/2	$\left(y_{i+1,j} - y_{i,j}\right)$	$\left(x_{i,j} - x_{i+1,j}\right)$
i+1/2,j	$\left(y_{i+1,j+1} - y_{i+1,j}\right)$	$\left(x_{i+1,j} - x_{i+1,j+1}\right)$
i,j+1/2	$\left(y_{i,j+1} - y_{i+1,j+1}\right)$	$\left(x_{i+1,j+1} - x_{i,j+1}\right)$
i-1/2,j	$\left(y_{i,j} - y_{i,j+1}\right)$	$\left(x_{i,j+1} - x_{i,j}\right)$

Table 2: Initial conditions to the blunt body problem

Property	Value
$M_{initial}$	8.78
$\rho_{initial}$	0.00326 kg/m^3
$pr_{initial}$	687 Pa
$U_{initial}$	4,776 m/s
$T_{initial}$	694 K
$T_{V,initial}$	694 K
T_{REF}	0 K
Altitude	40,000 m
c_N	10^{-9}
c_O	0.07955
c_{O2}	0.13400
c_{NO}	0.05090
L_{char}	2.0 m
Re_{char}	2.386x10^6
$B_{y,initial}$	0.15 T
$\mu_{M,char}$	1.2566x10^{-6}T.m/A
σ_{char}	1,000 ohm/m

Table 3: Initial conditions to the double ellipse problem

Property	Value
$M_{initial}$	15.0
$\rho_{initial}$	0.00922 kg/m^3
$pr_{initial}$	794 Pa
$U_{initial}$	5,208 m/s
$T_{initial}$	300 K
$T_{V,initial}$	300 K
T_{REF}	0 K
Altitude	50,000 m
c_N	10^{-9}
c_O	0.07955
c_{O2}	0.13400
c_{NO}	0.05090
L_{char}	5.0 m
Re_{char}	1.574x10^6
$B_{y,initial}$	0.15 T
$\mu_{M,char}$	1.2566x10^{-6}T.m/A
σ_{char}	1,000 ohm/m

Table 4: Initial conditions to the reentry capsule problem

Property	Value
$M_{initial}$	10.6
$\rho_{initial}$	0.02863 kg/m^3
$pr_{initial}$	3,885 Pa
$U_{initial}$	4,628 m/s
$T_{initial}$	473 K
$T_{V,initial}$	473 K
T_{REF}	0 K
Altitude	40,000 m
c_N	10^{-9}
c_O	0.07955
c_{O2}	0.13400
c_{NO}	0.05090
L_{char}	3.0 m
Re_{char}	$3.468x10^6$
$B_{y,initial}$	0.15 T
$\mu_{M,char}$	$1.2566x10^{-6}$T.m/A
σ_{char}	1,000 ohm/m

Table 5: Values of theoretical stagnation pressure

Problem:	$M_{initial}$:	pr_0/pr_∞:	pr_∞:	pr_0 (Theoretical):
Blunt body	8.78	99.98	1.709	170.87
Double ellipse	15.00	290.20	7.109	2,063.03
Reentry capsule	10.60	145.46	9.664	1,405.73

Table 6: Values of stagnation pressure and respective errors (Inviscid case/5th Order)

Physical Problem:	Spectral Method:	pr_0: (Numerical)	Error:
Blunt Body (pr_0 = 170.87)	Chebyshev-Gauss-Radau	103.24	39.58
	Chebyshev-Gauss-Lobatto	96.44	43.56
	Legendre-Gauss-Radau	84.56	50.51
	Legendre-Gauss-Lobatto	80.57	52.85
Reentry Capsule (pr_0 = 1,405.73)	Chebyshev-Gauss-Radau	1,353.42	3.72
	Chebyshev-Gauss-Lobatto	1,286.38	8.49
	Legendre-Gauss-Radau	1,160.37	17.45
	Legendre-Gauss-Lobatto	1,118.89	20.41

Table 7: Values of stagnation pressure and respective errors (Viscous case/8th Order)

Physical Problem:	Spectral Method:	pr_0: (Numerical)	Error:
Blunt Body (pr_0 = 170.87)	Chebyshev-Gauss-Radau	170.05	0.48
	Chebyshev-Gauss-Lobatto	164.87	3.51
	Legendre-Gauss-Radau	145.91	14.61
	Legendre-Gauss-Lobatto	146.41	14.31
Double Ellipse (pr_0 = 2,063.03)	Chebyshev-Gauss-Radau	1,959.25	5.03
	Chebyshev-Gauss-Lobatto	1,902.12	7.80
	Legendre-Gauss-Radau	1,662.31	19.42
	Legendre-Gauss-Lobatto	1,667.46	19.17

Table 8: Values of the lift aerodynamic coefficient (Inviscid case/5th Order)

Physical Problem:	Spectral Method:	c_L:
Blunt Body	Chebyshev-Gauss-Radau	$-8.7244x10^{-16}$
	Chebyshev-Gauss-Lobatto	$1.2550x10^{-15}$

	Legendre-Gauss-Radau	$4.8328x10^{-16}$
	Legendre-Gauss-Lobatto	$-4.7984x10^{-16}$
	Chebyshev-Gauss-Radau	$-2.2224x10^{-09}$
Reentry Capsule	Chebyshev-Gauss-Lobatto	$-2.2505x10^{-09}$
	Legendre-Gauss-Radau	$-2.1593x10^{-09}$
	Legendre-Gauss-Lobatto	$-2.1376x10^{-09}$

Table 9: Values of the lift aerodynamic coefficient (Viscous case/8th Order)

Physical Problem:	**Spectral Method:**	**c_L:**
	Chebyshev-Gauss-Radau	$1.3765x10^{-16}$
Blunt Body	Chebyshev-Gauss-Lobatto	$6.3714x10^{-17}$
	Legendre-Gauss-Radau	$-4.9929x10^{-16}$
	Legendre-Gauss-Lobatto	$1.0163x10^{-16}$

Table 10: Computational data (Inviscid case/5th Order)

Physical Problem:	**Spectral Method:**	**CFL:**	**Iterations:**
	Chebyshev-Gauss-Radau	0.10	3,224
Blunt Body	Chebyshev-Gauss-Lobatto	0.10	1,554
	Legendre-Gauss-Radau	0.10	1,147
	Legendre-Gauss-Lobatto	0.10	1,375
	Chebyshev-Gauss-Radau	0.06	3,965
Reentry Capsule	Chebyshev-Gauss-Lobatto	0.05	3,911
	Legendre-Gauss-Radau	0.03	4,547
	Legendre-Gauss-Lobatto	0.03	4,033

Table 11: Computational data (Viscous case/8th Order)

Physical Problem:	**Spectral Method:**	**CFL:**	**Iterations:**
	Chebyshev-Gauss-Radau	0.10	3,011
Blunt Body	Chebyshev-Gauss-Lobatto	0.10	2,662
	Legendre-Gauss-Radau	0.10	1,569
	Legendre-Gauss-Lobatto	0.10	1,593
	Chebyshev-Gauss-Radau	0.05	9,618
Double Ellipse	Chebyshev-Gauss-Lobatto	0.08	5,373
	Legendre-Gauss-Radau	0.01	27,686
	Legendre-Gauss-Lobatto	0.01	27,985

Table 12: Computational cost of spectral variants

Order of Accuracy:	**Spectral Method:**	**Computational Cost (seconds/volumes/iterations):**
	Chebyshev-Gauss-Radau	0.00022995
5th Order	Chebyshev-Gauss-Lobatto	0.00017704
(Inviscid case)	Legendre-Gauss-Radau	0.00017724
	Legendre-Gauss-Lobatto	0.00022635
	Chebyshev-Gauss-Radau	0.00052307
8th Order	Chebyshev-Gauss-Lobatto	0.00042166
(Viscous case)	Legendre-Gauss-Radau	0.00042148
	Legendre-Gauss-Lobatto	0.00053265

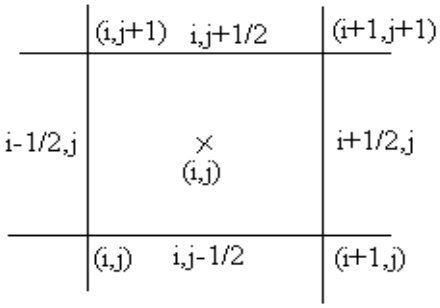

Figure 1: Computational cell

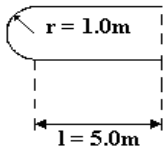

Figure 2: Bluntbody configuration

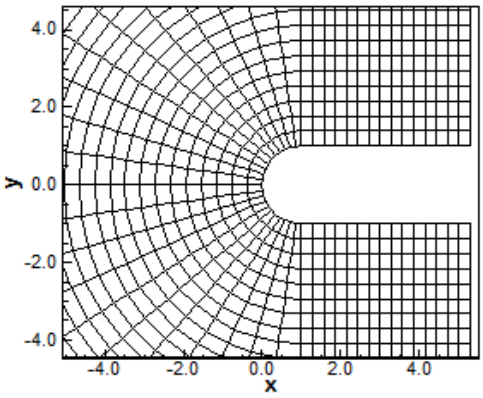

Figure 3: Blunt body inviscid mesh

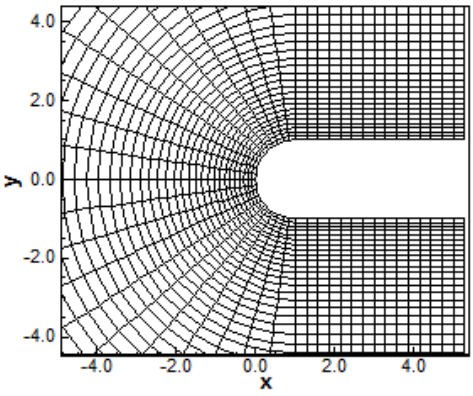

Figure 4: Blunt body viscous mesh

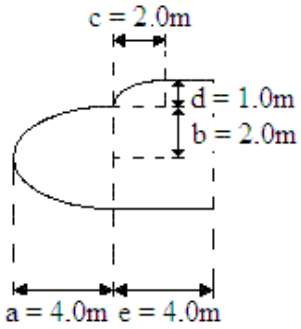

Figure 5: Double ellipse configuration

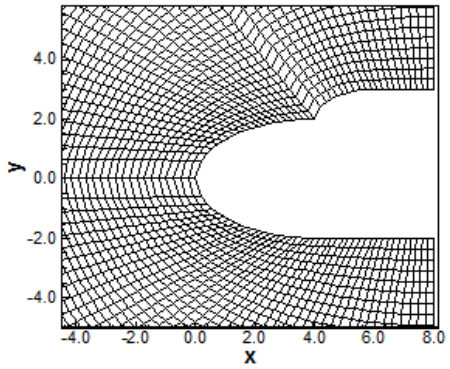

Figure 6: Double ellipse inviscid mesh

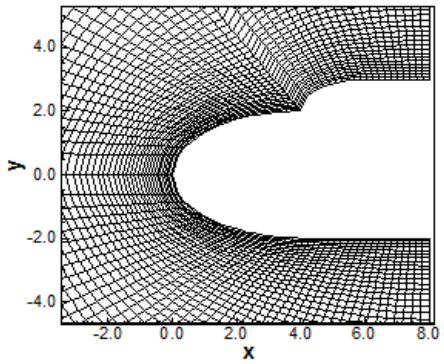

Figure 7: Double ellipse viscous mesh

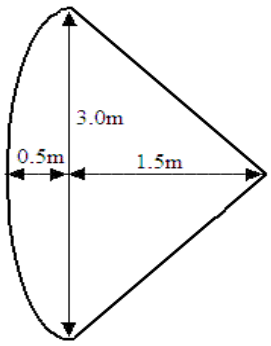

Figure 8: Reentry capsule configuration

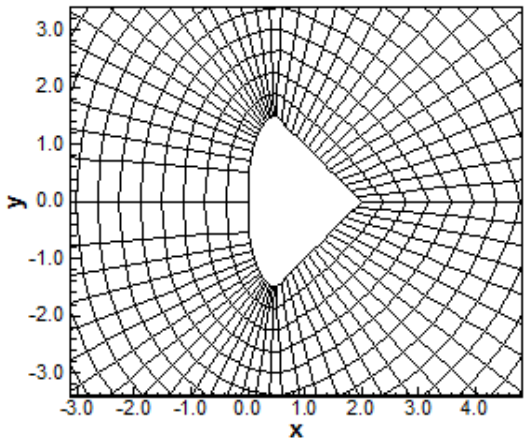

Figure 9: Reentry capsule inviscid mesh

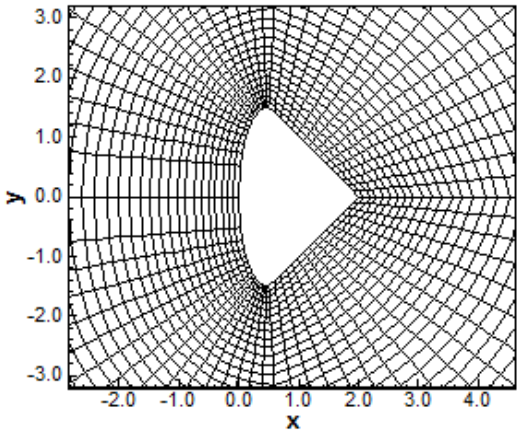

Figure 10: Reentry capsule viscous mesh

BLUNT BODY INVISCID SOLUTIONS

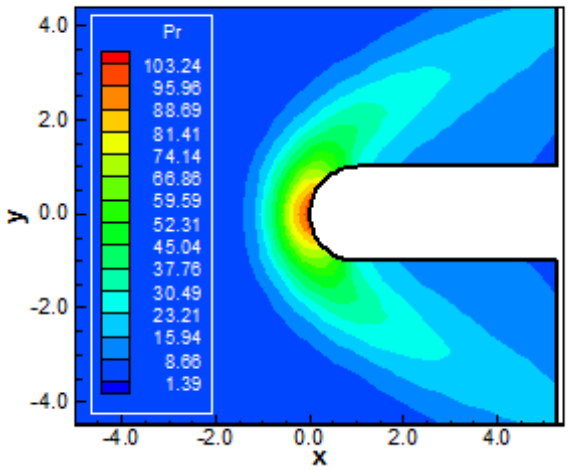

Figure 11: Pressure contours (CGR-5th)

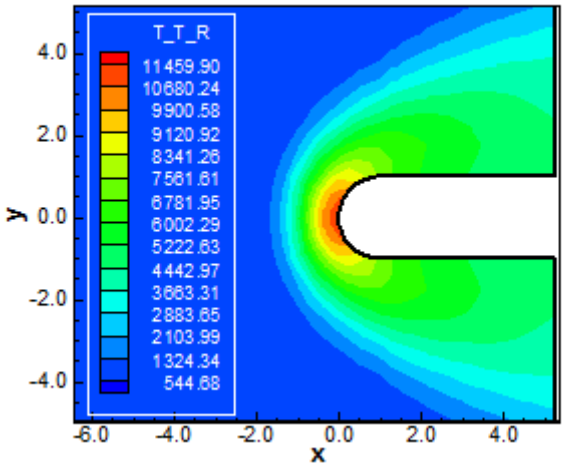

Figure 12: Translational/rotational temperature contours (CGR-5th)

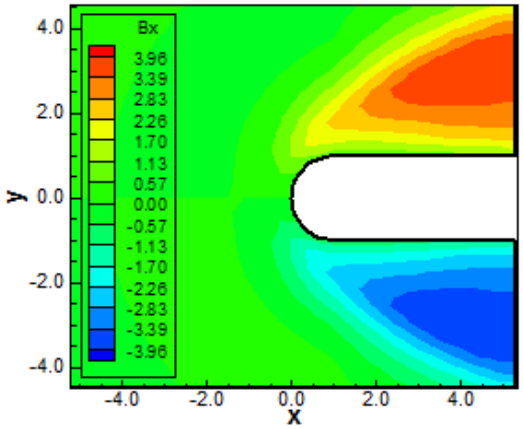

Figure 13: B_x component of the magnetic field (CGR-5th)

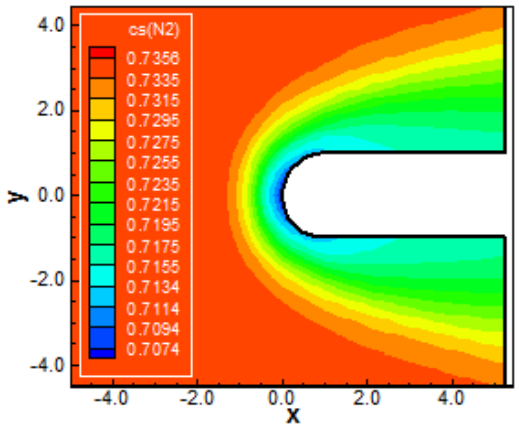

Figure 14: N_2 mass fraction contours (CGR-5th)

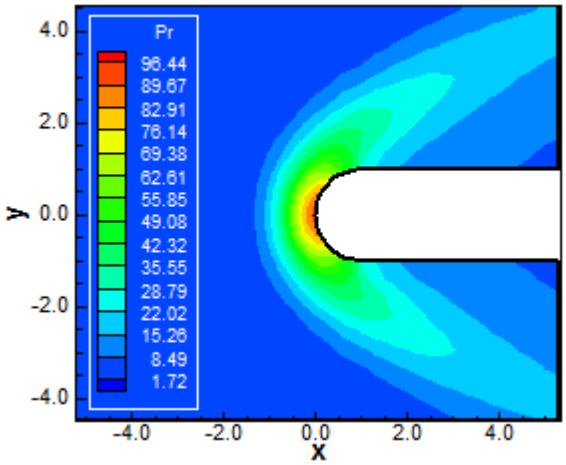

Figure 15: Pressure contours (CGL-5th)

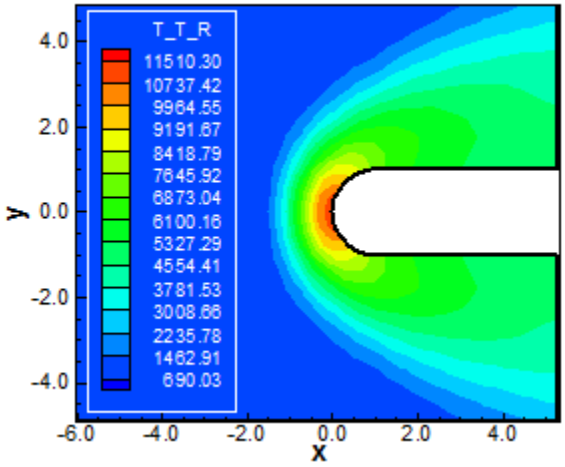

Figure 16: Translational/rotational temperature contours (CGL-5th)

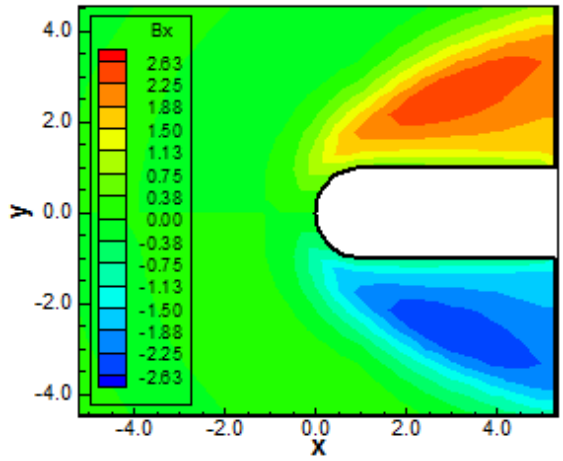

Figure 17: B_x component of the magnetic field (CGL-5th)

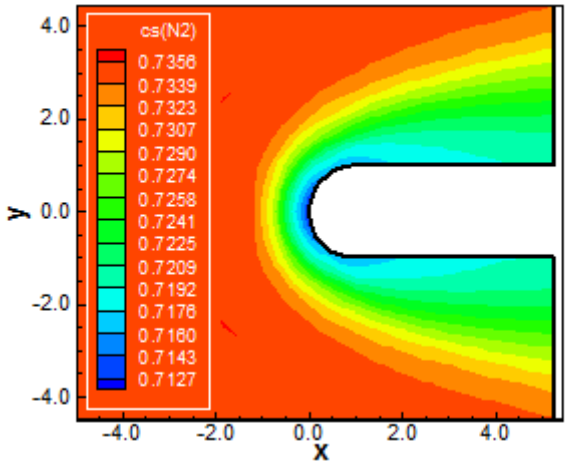

Figure 18: N_2 mass fraction contours (CGL-5th)

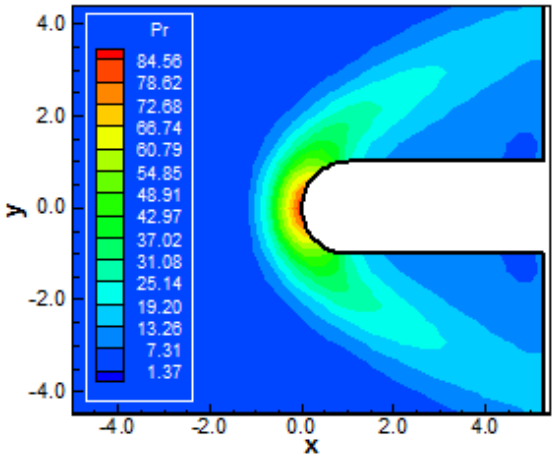

Figure 19: Pressure contours (LGR-5th)

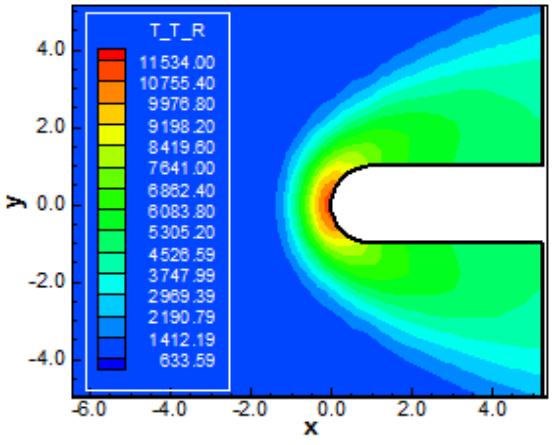

Figure 20: Translational/rotational temperature contours (LGR-5th)

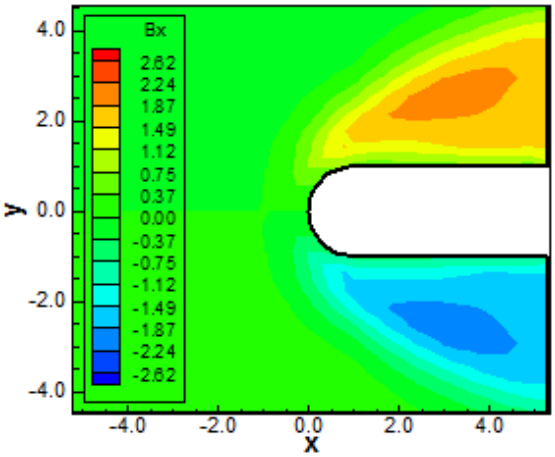

Figure 21: B_x component of the magnetic field (LGR-5th)

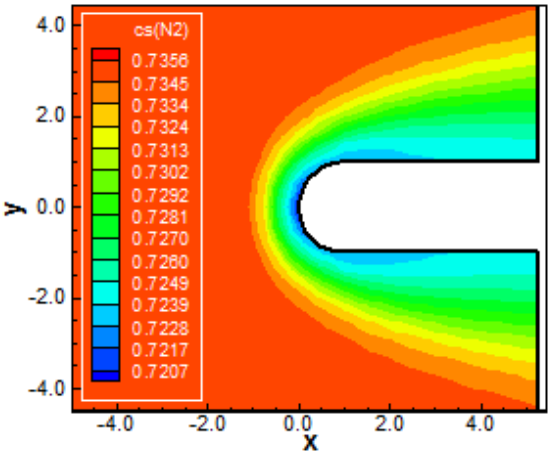

Figure 22: N_2 mass fraction contours (LGR-5th)

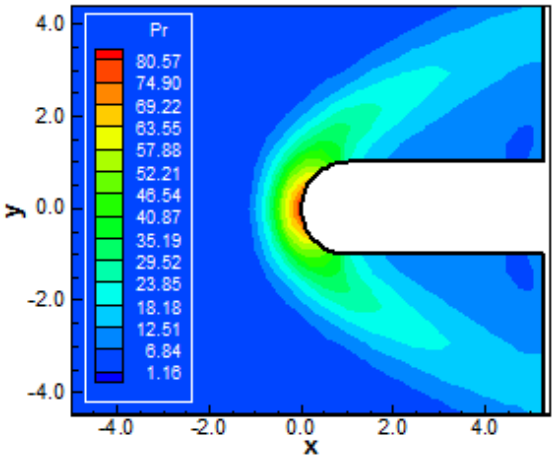

Figure 23: Pressure contours (LGL-5th)

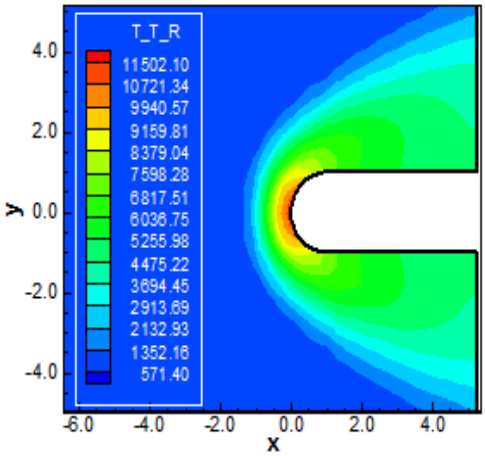

Figure 24: Translational/rotational temperature contours (LGL-5th)

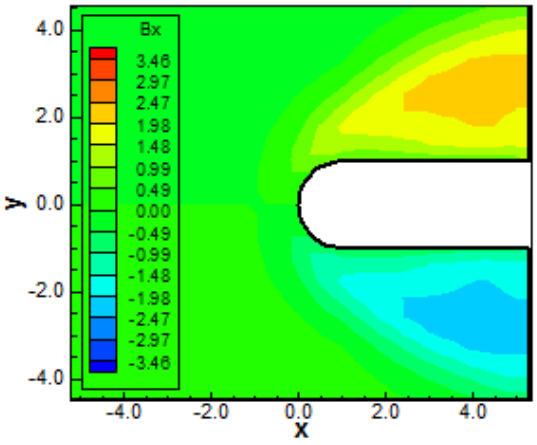

Figure 25: B_x component of the magnetic field (LGL-5th)

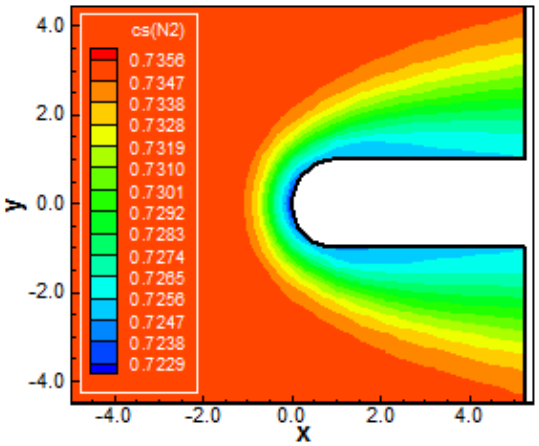

Figure 26: N_2 mass fraction contours (LGL-5th)

BLUNT BODY VISCOUS SOLUTIONS

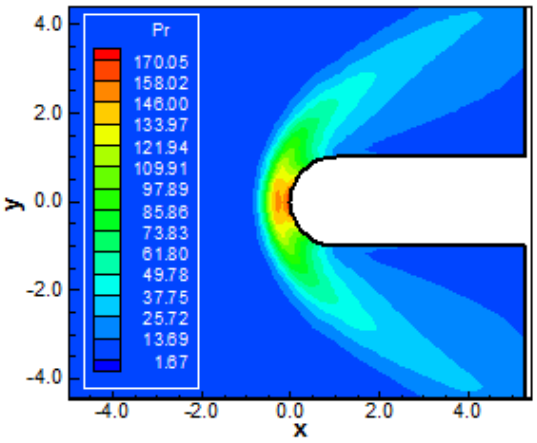

Figure 27: Pressure contours (CGR-8th)

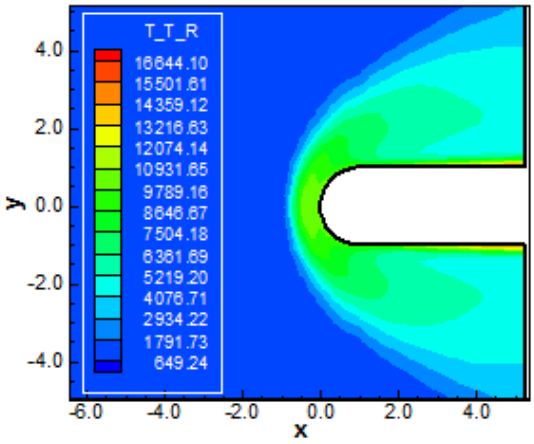

Figure 28: Translational/rotational temperature contours (CGR-8th)

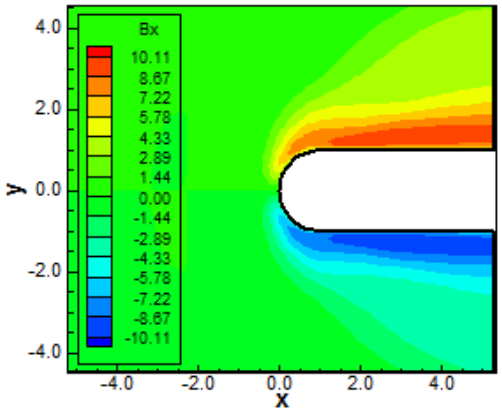

Figure 29: B_x component of the magnetic field (CGR-8th)

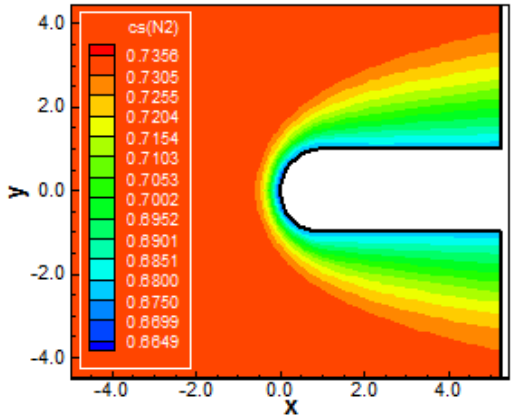

Figure 30: N_2 mass fraction contours (CGR-8th)

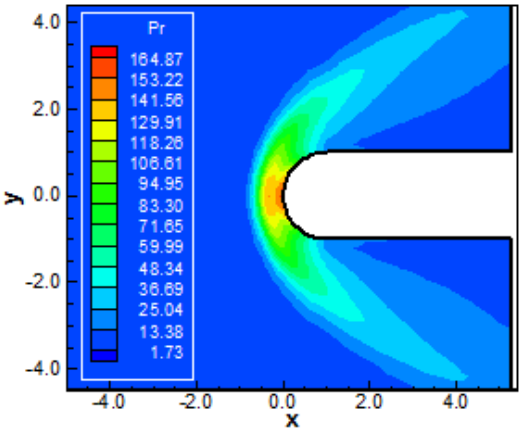

Figure 31: Pressure contours (CGL-8th)

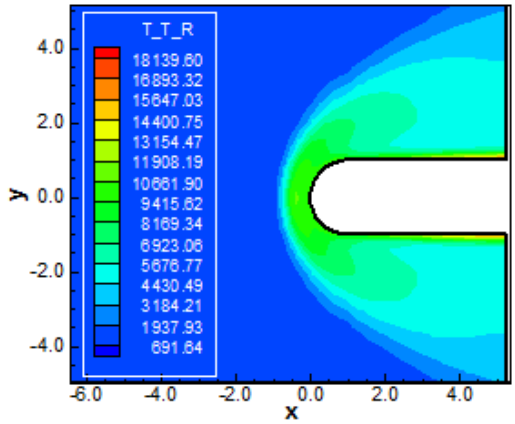

Figure 32: Translational/rotational temperature contours (CGL-8th)

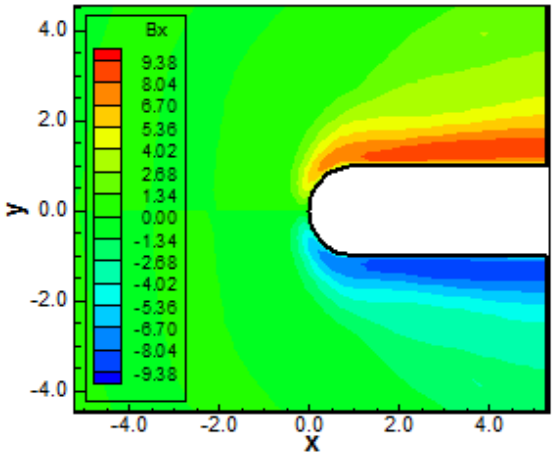

Figure 33: B_x component of the magnetic field (CGL-8th)

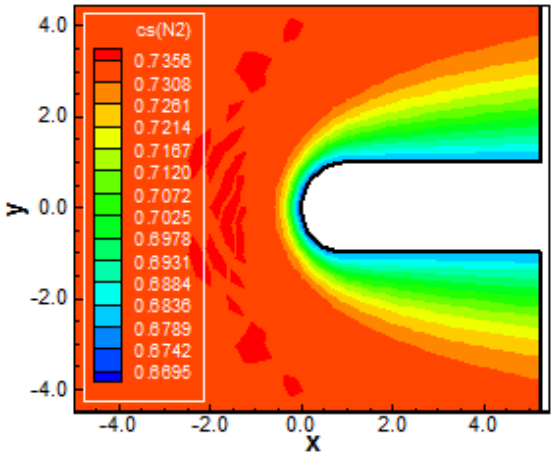

Figure 34: N_2 mass fraction contours (CGL-8th)

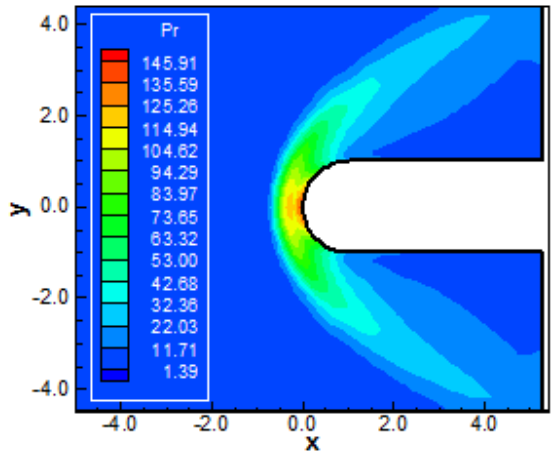

Figure 35: Pressure contours (LGR-8th)

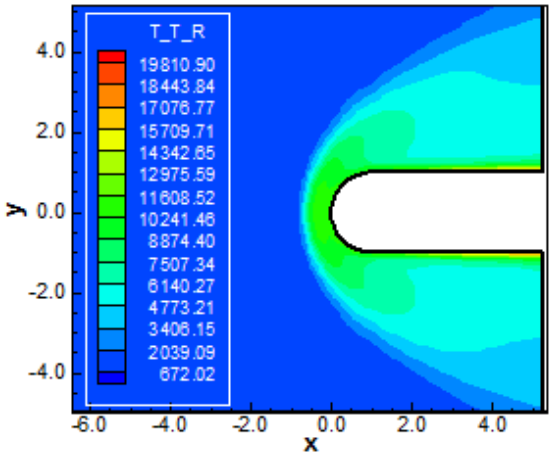

Figure 36: Translational/rotational temperature contours (LGR-8th)

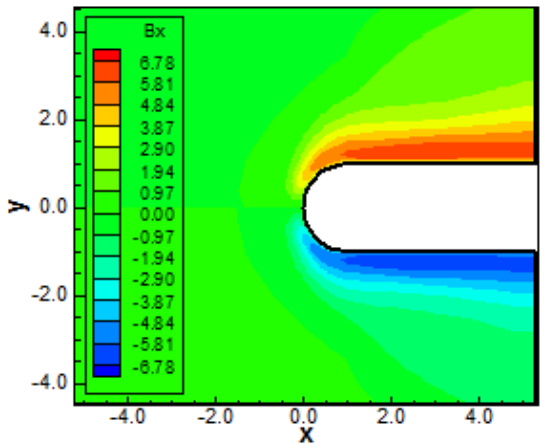

Figure 37: B_x component of the magnetic field (LGR-8th)

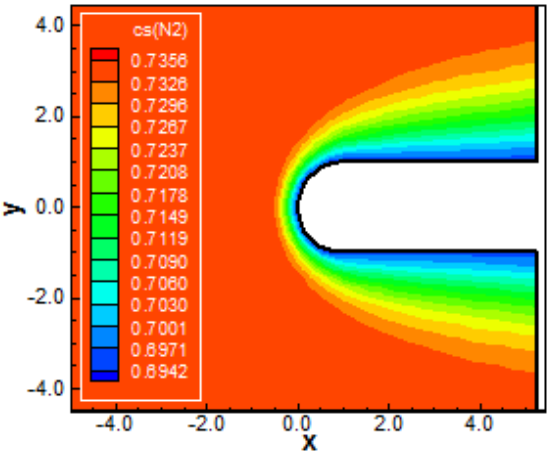

Figure 38: N_2 mass fraction contours (LGR-8th)

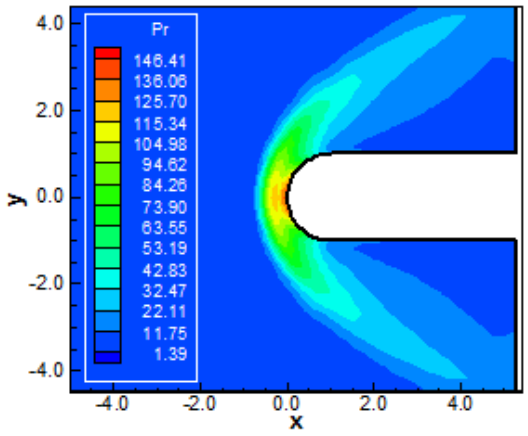

Figure 39: Pressure contours (LGL-8th)

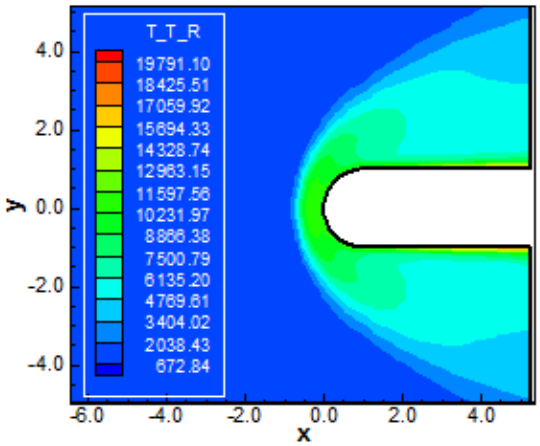

Figure 40: Translational/rotational temperature contours (LGL-8th)

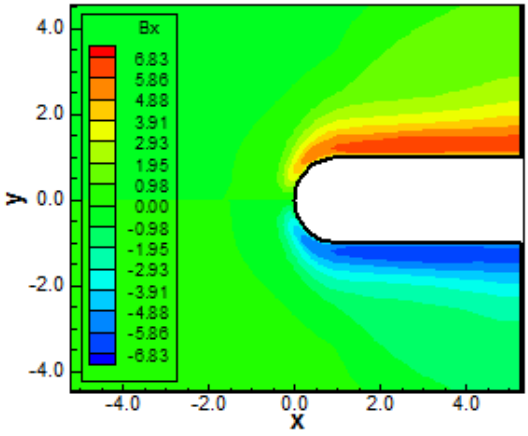

Figure 41: B_x component of the magnetic field (LGL-8th)

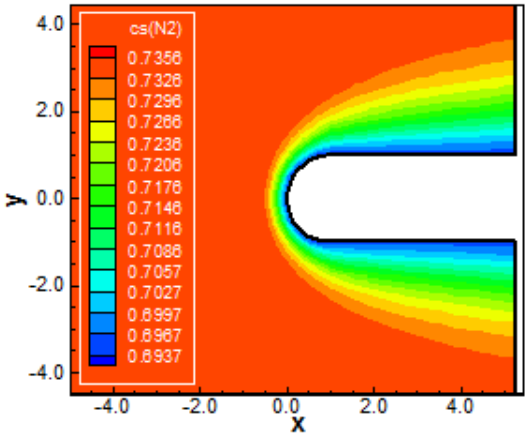

Figure 42: N_2 mass fraction contours (LGL-8th)

DOUBLE ELLIPSE VISCOUS SOLUTIONS

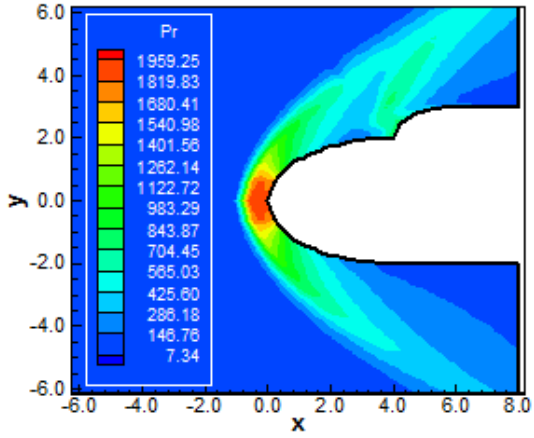

Figure 43: Pressure contours (CGR-8th)

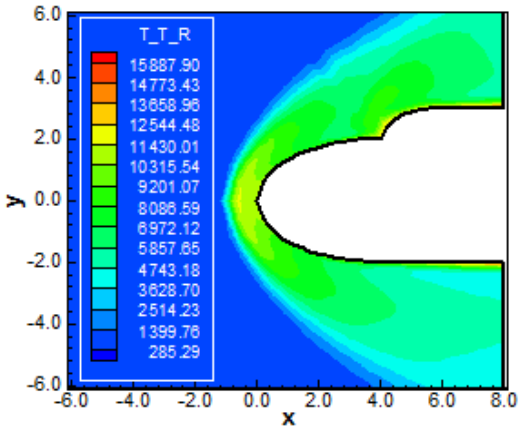

Figure 44: Translational/rotational temperature contours (CGR-8th)

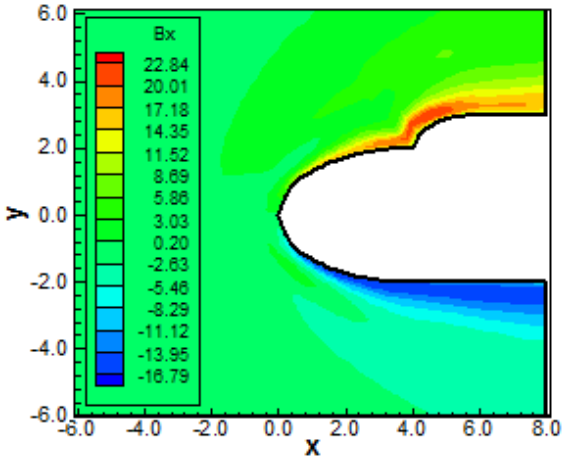

Figure 45: B_x component of the magnetic field (CGR-8th)

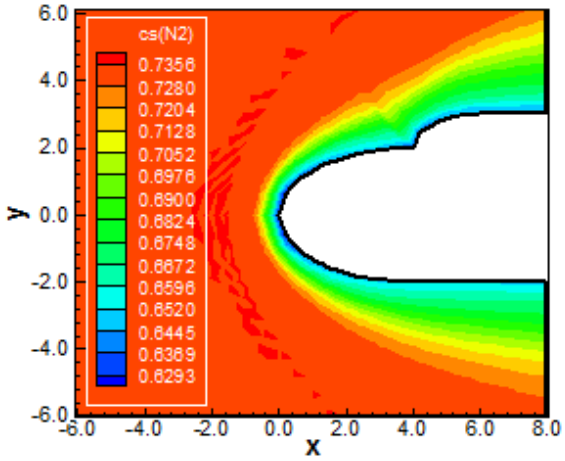

Figure 46: N_2 mass fraction contours (CGR-8th)

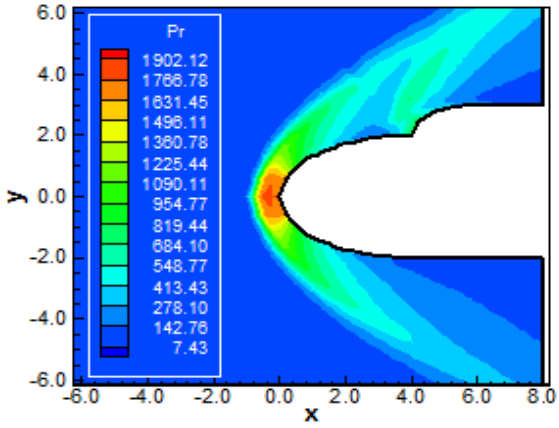

Figure 47: Pressure contours (CGL-8th)

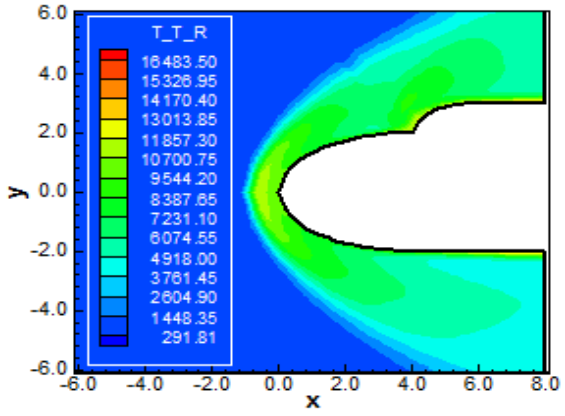

Figure 48: Translational/rotational temperature contours (CGL-8th)

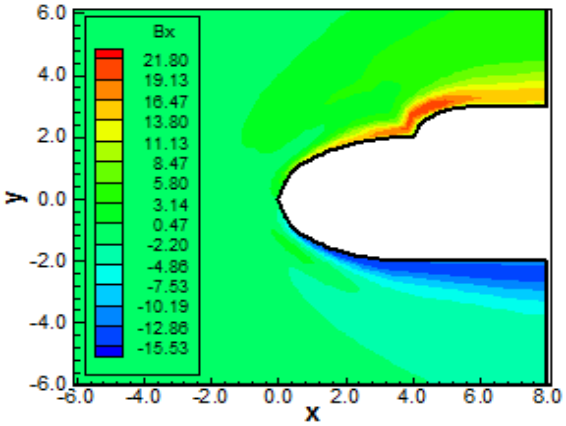

Figure 49: B_x component of the magnetic field (CGL-8th)

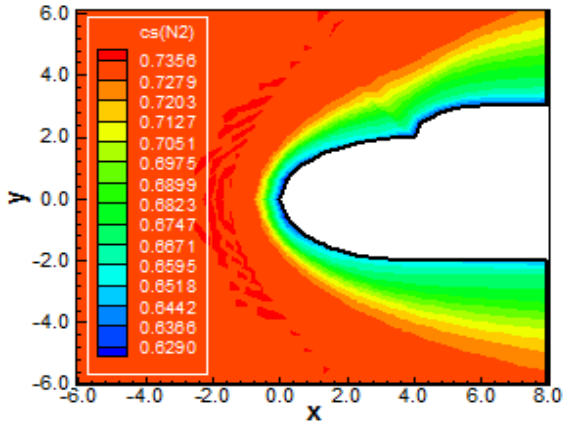

Figure 50: N_2 mass fraction contours (CGL-8th).

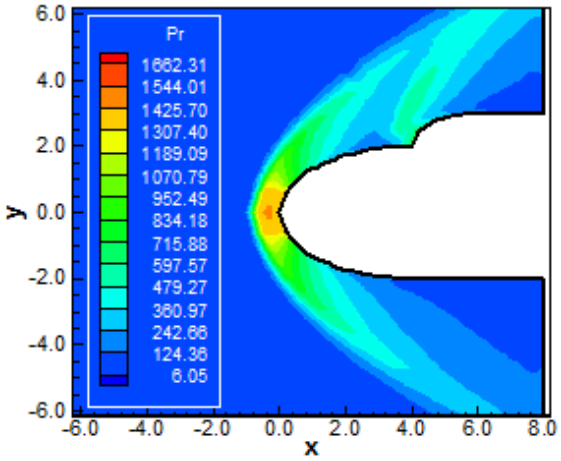

Figure 51: Pressure contours (LGR-8th)

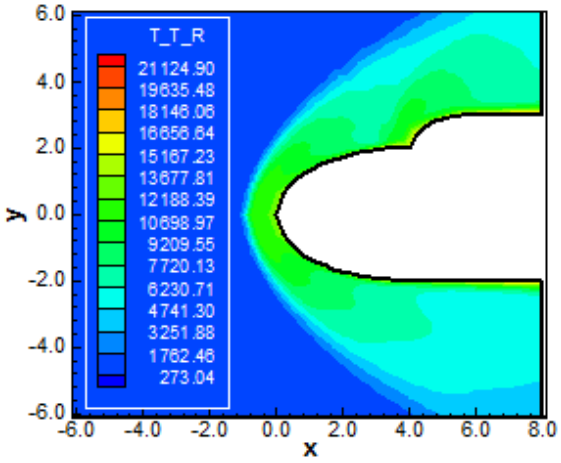

Figure 52: Translational/rotational temperature contours (LGR-8th)

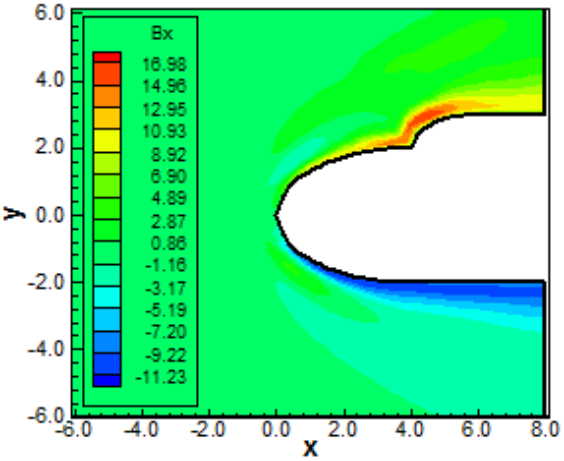

Figure 53: B_x component of the magnetic field (LGR-8th)

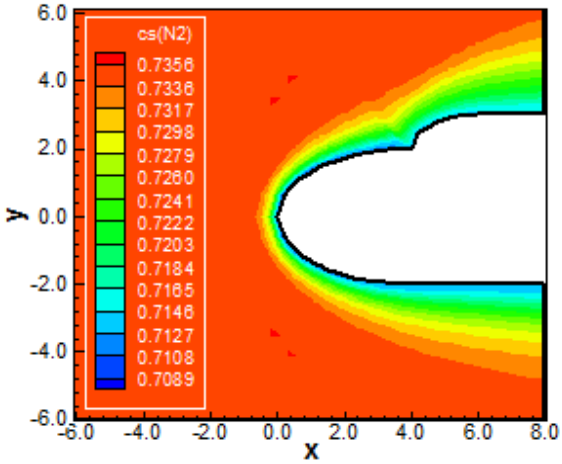

Figure 54: N_2 mass fraction contours (LGR-8th)

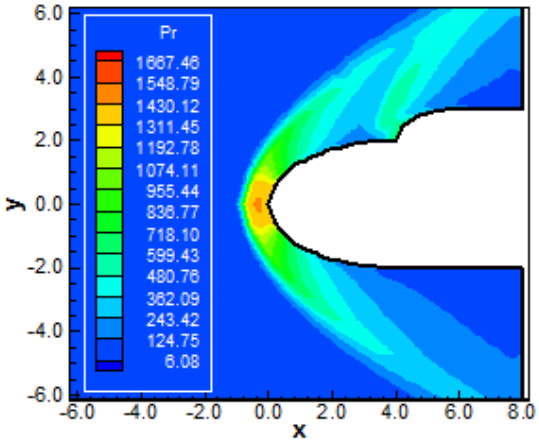

Figure 55: Pressure contours (LGL-8th)

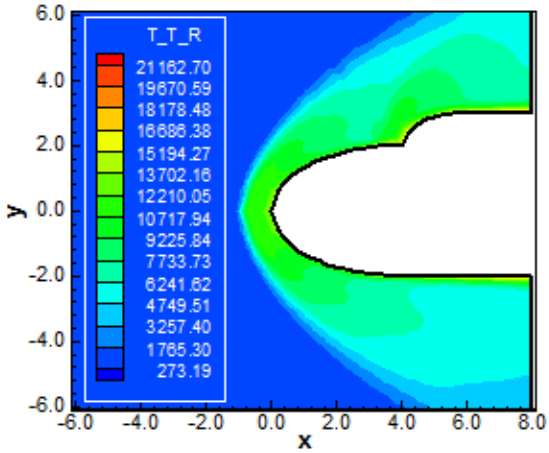

Figure 56: Translational/rotational temperature contours (LGL-8th)

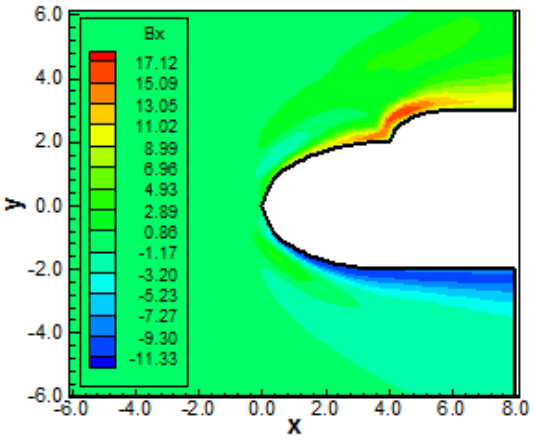

Figure 57: B_x component of the magnetic field (LGL-8th)

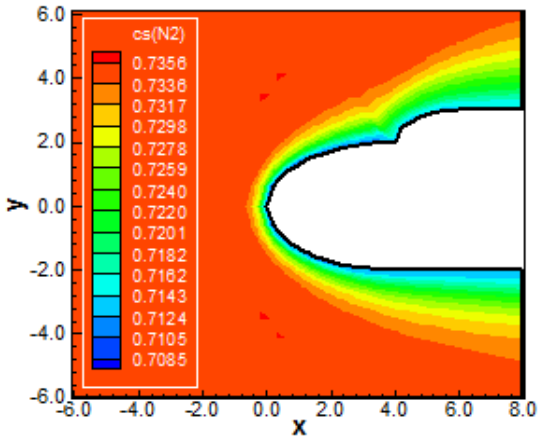

Figure 58: N_2 mass fraction contours (LGL-8th)

REENTRY CAPSULE INVISCID SOLUTIONS

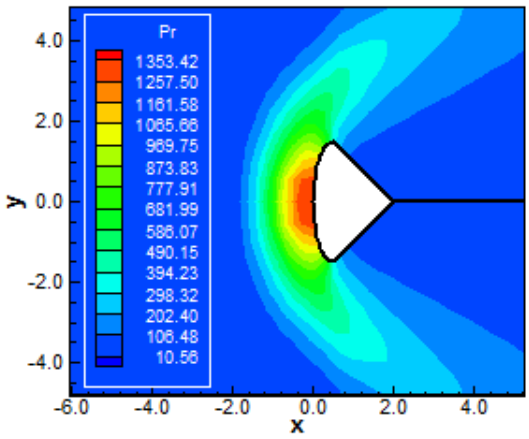

Figure 59: Pressure contours (CGR-5th)

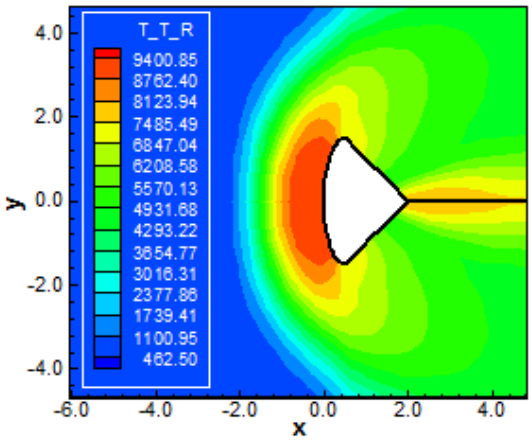

Figure 60: Translational/rotational temperature contours (CGR-5th)

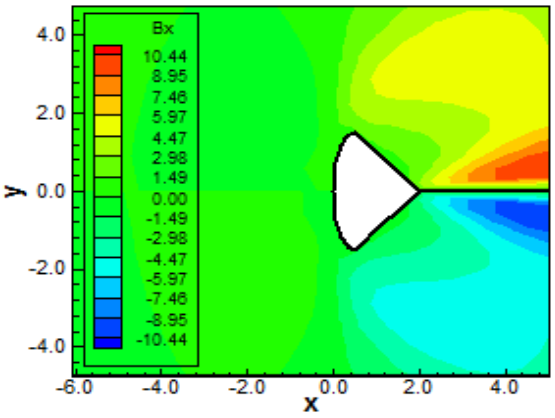

Figure 61: B_x component of the magnetic field (CGR-5th)

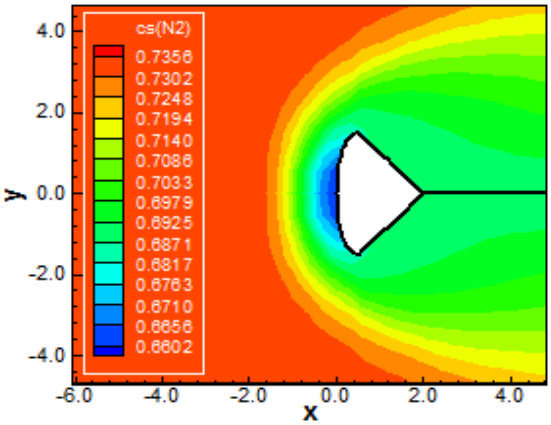

Figure 62: N_2 mass fraction contours (CGR-5th)

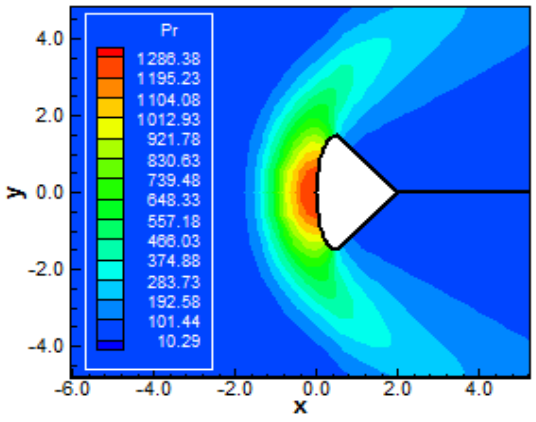

Figure 63: Pressure contours (CGL-5th)

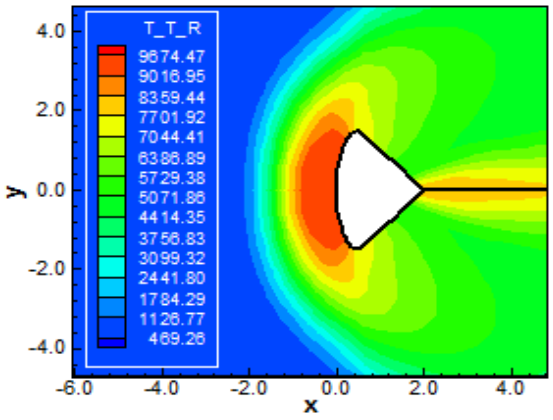

Figure 64: Translational/rotational temperature contours (CGL-5th)

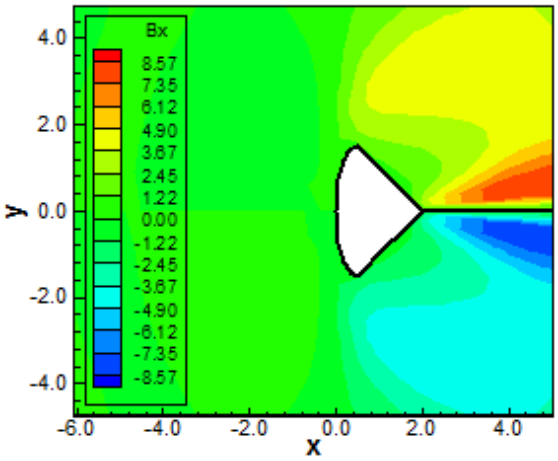

Figure 65: B_x component of the magnetic field (CGL-5th)

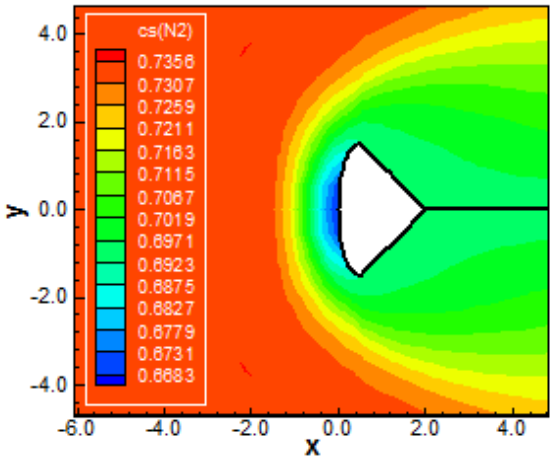

Figure 66: N_2 mass fraction contours (CGL-5th)

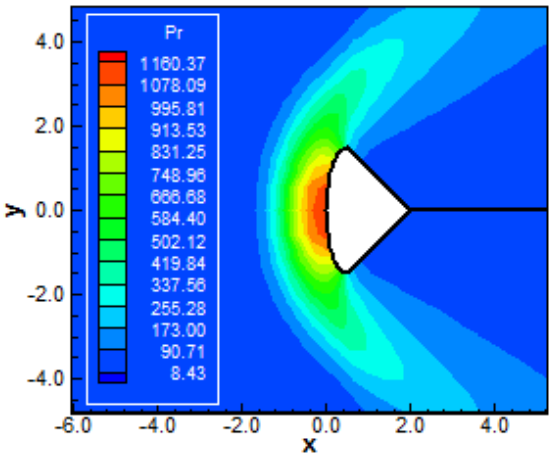

Figure 67: Pressure contours (LGR-5th)

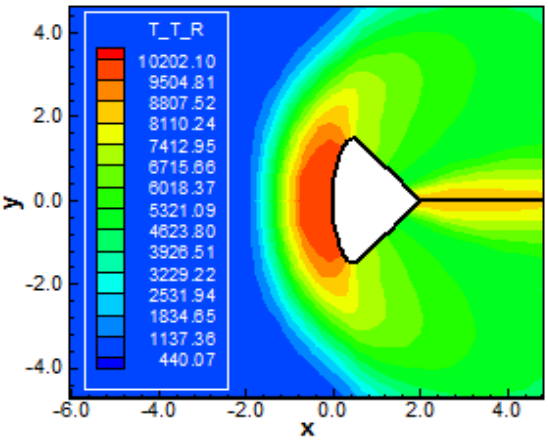

Figure 68: Translational/rotational temperature contours (LGR-5th)

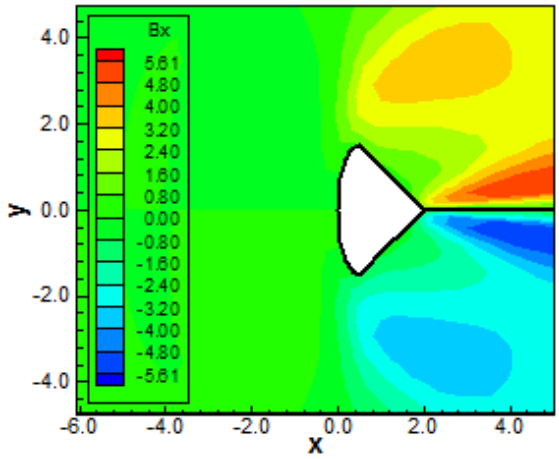

Figure 69: B_x component of the magnetic field (LGR-5th)

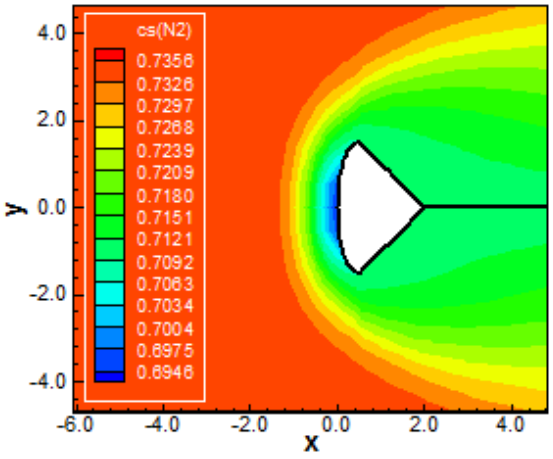

Figure 70: N_2 mass fraction contours (LGR-5th)

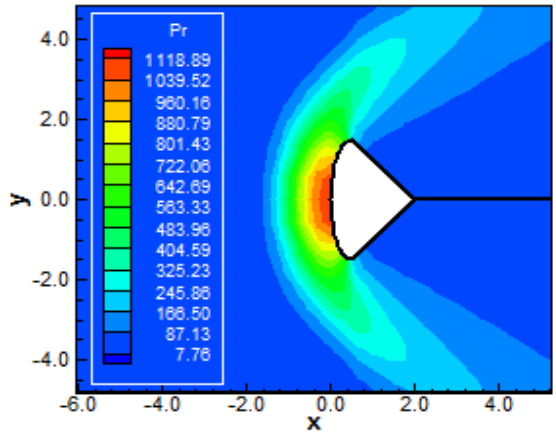

Figure 71: Pressure contours (LGL-5th)

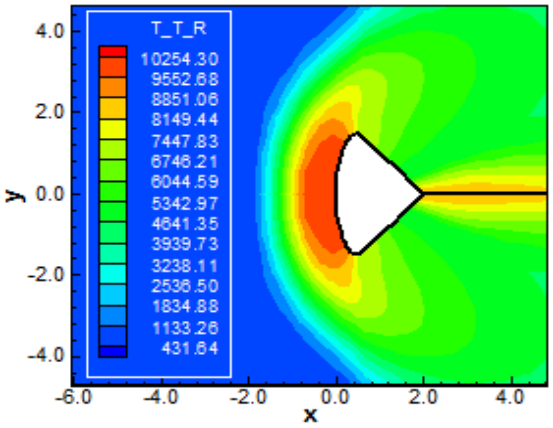

Figure 72: Translational/rotational temperature contours (LGL-5th)

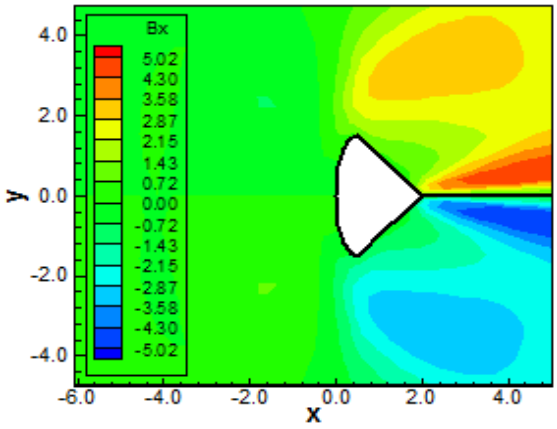

Figure 73: B_x component of the magnetic field (LGL-5th)

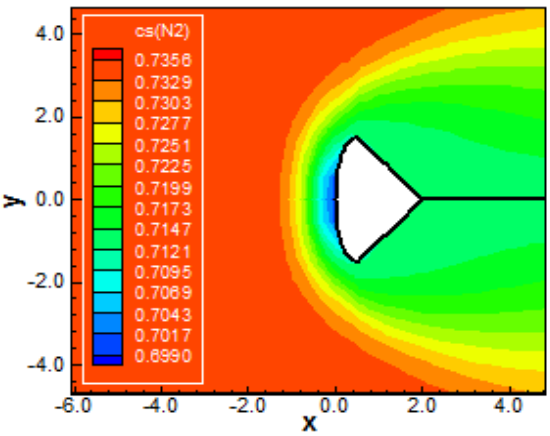

Figure 74: N_2 mass fraction contours (LGL-5th)

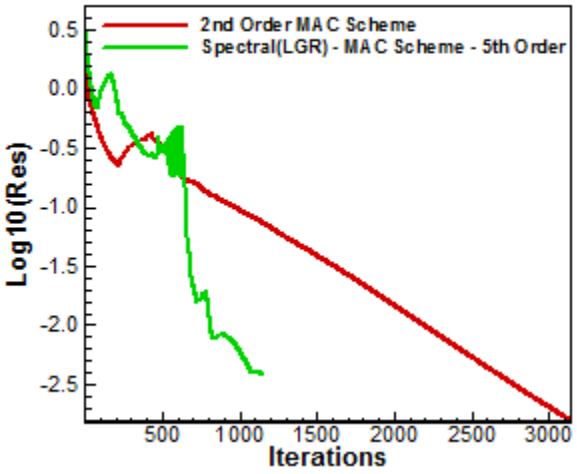

Figure 75: Convergence history comparison (Inviscid case)

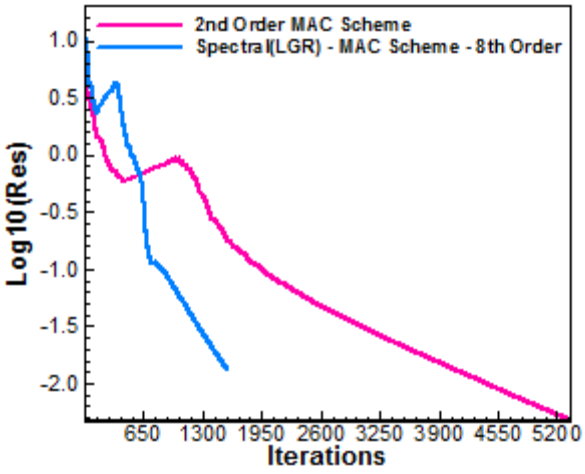

Figure 76: Convergence history comparison (Viscous case)

9. Conclusions

In the present work, a study involving a spectral method to solve the reactive Euler and Navier-Stokes equations submitted to a magnetic field was performed. The Euler and Navier-Stokes equations, coupled with the Maxwell equations, in conservative and finite volume contexts, employing structured spatial discretization, on a condition of thermochemical non-equilibrium, were studied. The spectral method presented in this work employed collocation points and variants of Chebyshev and Legendre interpolation functions were analyzed. The symmetrical algorithm of [35] was used to perform the reentry flow numerical experiments, which gave us an original contribution to the CFD community. The [36] artificial dissipation model was applied. The "hot gas" hypersonic flows around a blunt body, around a double ellipse, and around a reentry capsule in two-dimensions were simulated. The Euler backward integration method was employed to march the scheme in time. The convergence process was accelerated to steady state condition through a spatially variable time step procedure, which had proved effective gains in terms of computational acceleration [37-38]. The reactive simulations involved Earth atmosphere chemical model of five species and seventeen reactions, based on the [39] model. N, O, N_2, O_2, and NO species were used to accomplish the numerical comparisons. The work of [40] was the reference one to present the fluid dynamics and Maxwell equations of electromagnetism based on a conservative and finite volume formalisms. The results have indicated that the Chebyshev collocation point variants were more accurate in terms of stagnation pressure estimations in the viscous case. Errors inferior to 8.00% were found for this parameter in the viscous case, being 0.48% the best result. The Legendre collocation point variants were more accurate in terms of the lift coefficient estimations. Moreover, the Legendre collocation point variants were more computationally efficient and cheaper.

As final conclusion, it was possible to highlight that, for the blunt body problem, the [35] scheme in the viscous case using Chebyshev-Gauss-Radau collocation points had the best performance in estimating the stagnation pressure, and the lift aerodynamic coefficient was best estimated by the [35] scheme as using the Chebyshev-Gauss-Lobatto collocation points; for the double ellipse problem, the [35] scheme in the viscous case using Chebyshev-Gauss-Radau collocation points had the best performance in estimating the stagnation pressure; and finally, for the reentry capsule problem, the [35] scheme in the inviscid case using Chebyshev-Gauss-Radau collocation points had the best performance in estimating the stagnation pressure, and the lift aerodynamic coefficient was best estimated by the [35] scheme as using the Legendre-Gauss-Lobatto collocation points. Moreover, the best performance of the numerical schemes, for the 5^{th} order of accuracy, was due to the [35] one, when using the Legendre-Gauss-Radau collocation points, employing a CFL of 0.10, and converging in 1,147 iterations, in the blunt body problem, whereas for the 8^{th} order of accuracy, the best performance of the numerical scheme was due to the [35] one, when using the Legendre-Gauss-Radau collocation points,

employing a CFL of 0.10, and converging in 1,569 iterations, also in the blunt body problem.

Finally, to close this work, the computational cost of the numerical schemes using the several types of collocation points was presented in Tab. 12. For the inviscid case, the cheapest combination was the [35] scheme using Chebyshev-Gauss-Lobatto collocation points with a cost of 0.00017704 sec/per-volume/per-iteration, whereas for the viscous case the cheapest was due to the [35] scheme coupled with the Legendre-Gauss-Radau collocation points with a cost of 0.00042148 sec/per-volume/per-iteration.

References

[1]. Barnes CJ, Huang GP, Shang JS. A high resolution spectral method for the compressible Navier-Stokes equations. AIAA Paper 2011-0049; 2011.

[2]. Huang P, Wang ZJ, Liu Y. An implicit space-time spectral difference method for discontinuity capturing using adaptive polynomials. AIAA Paper 2005-5255; 2005.

[3]. Huang P. High order discontinuity capturing using adaptive polynomials. AIAA Paper 2006-0305; 2006.

[4]. Steger JL, Warming RF. Flux vector splitting of the inviscid gas dynamic equations with application to finite difference methods. Journal of Computational Physics. 1981; 40: 263-293.

[5]. Hughes T. The finite element method, linear static and dynamic finite element analysis, Prentice-Hall, Inc.

[6]. Lele S. Compact finite difference schemes with spectral-like resolution. Journal of Computational Physics.1991; 103: 16-42.

[7]. Gottlieb D, Orszag S. Numerical analysis of spectral methods: theory and applications. Society for industrial and applied mathematics, Philadelphia.

[8]. Hussaini MY, Kopriva DA, Salas MD, Zang TA. Spectral methods for the Euler equations: Part I – Fourier methods and shock capturing. AIAA Journal. 1985; 23(1): 64-70.

[9]. Slater JC. Electronic energy bands in metal. Physical Review.1934; 45: 794-801.

[10]. BartaJ. Ü ber die naherungsweise l ü sung einigerzweidimensionalerelastizit ä tsaufgaben. Zeitschriftfuer Angewandte Mathematik und Mechanik.1937; 17: 184-185.

[11]. Frazer RA, Jones WP, SkanSW. Approximation to functions and to the solutions of differential equations. Aeronautical Research Council, London. R&M 1799; 1937.

[12]. Lanczos CL. Trigonometric interpolation of empirical and analytic functions. Journal of Mathematics and Physics.1938; 17: 123-199.

[13]. Gottlieb D, Lustman L, Orszag SA. Spectral calculations of one-dimensional inviscid compressible flows. SIAM Journal of Scientific and Statistical Computation.1981; 2: 296-310.

[14]. Taylor TD, Meyers RB, Albert JH. Pseudospectral calculations of shock waves, rarefaction waves and contact surfaces. Computers and Fluids.1981; 9: 469-473.

[15]. Zang TA, Hussaini MY. Mixed spectral-finite difference approximations for slightly viscous flows. Proceedings of the 7th International Conference on Numerical Methods in Fluid Dynamics. Edited by W. C. Reynolds and R. W. MacCormack. Lecture Notes in Physics.1981; (141): 461-466.

[16]. Narayan JR, Girimaji SS. Turbulent reacting flow computations including turbulence-chemistry interactions. AIAA Paper 92-0342; 1992.

[17]. Gnoffo PA, Gupta RN, Shinn JL. Conservation equations and physical models for hypersonic flows in thermal and chemical nonequilibrium. NASA TP 2867; 1989.

[18]. Liu M, Vinokur M. Upwind algorithms for general thermo-chemical nonequilibrium flows. AIAA Paper 89-0201; 1989.

[19]. Park C. Radiation enhancement by nonequilibrium in Earth's atmosphere. Journal of Spacecraft and Rockets.1985; 22(1): 27-36.

[20]. Park C. Problem of rate chemistry in the flight regimes of aeroassissted orbital transfer vehicles. Thermal design of aeroassissted orbital transfer vehicles. Progress in Astronautics and Aeronautics. Edited by H. F. Nelson, AIAA, NY.1985; 96: 511-537.

[21]. GnoffoPA. Three-dimensional AOTV flow fields in chemical nonequilibrium. AIAA Paper 86-0230; 1986.
[22]. Li CP. Implicit methods for computing chemically reacting flow. NASA TM-58274; 1986.
[23]. Lee JH. Basic governing equations for the flight regimes of aeroassisted orbital transfer vehicles. Thermal design of aeroassisted transfer vehicles. Progress in Astronautics and Aeronautics, AIAA.1985; 96: 3-53.
[24]. Park C. Convergence of computation of chemically reacting flows. Thermophysical aspects of reentry flows. Progress in Astronautics and Aeronautics. Edited by J. N. Moss and C. D. Scott, AIAA, NY.1986; 103: 478-513.
[25]. Park C. Assessment of two-temperature kinetic model for dissociating and weakly-ionizing nitrogen. AIAA Paper 86-1347; 1986.
[26]. Park C. Calculation of nonequilibrium radiation in the flight regimes of aeroassissted orbital transfer vehicles. Thermal design of aeroassissted orbital transfer vehicles. Progress in Astronautics and Aeronautics. Edited by H. F. Nelson, AIAA, NY.1985; 96: 395-418.
[27]. Park C. Nonequilibrium air radiation (NEQAIR) program: User's manual. NASA TM-86707; 1985.
[28]. Davidson PA. Magnetohydrodynamics in materials processing. Ann. Rev. Fluid Mech.1999; 31: 273-300.
[29]. Ziemer RW, Bush WB. Magnetic field effects on bow shock stand-off distance. Physical Review Letters.1958; 1(2): 58-59.
[30]. Meyer RX. Magnetohydrodynamics and aerodynamic heating. ARS Journal.1959; 29(3): 187-192.
[31]. Gurijanov EP, Harsha PT. AJAX: New directions in hypersonic technology. AIAA Paper 96-4609; 1996.
[32]. Brichkin DI, Kuranov AL, Sheikin EG. MHD-technology for scramjet control. AIAA Paper 98-1642; 1998.
[33]. Ganiev YC, Gordeev VP, Krasilnikov AV, Lagutin VI, Otmennikov VN, Panasenko AV. Theoretical and experimental study of the possibility of reducing aerodynamic drag by employing plasma injection. AIAA Paper 99-0603; 1999.
[34]. Adamovich IV, Subramanian VV, Rich JW, Macheret SO. Phenomenological analysis of shock-wave propagation in weakly ionized plasmas. AIAA Journal.1998; 36(5): 816-822
[35]. Maciel ESG. Magnetic field applied to thermochemical non-equilibrium reentry flows in 2D - Five species. International Journal of Computational Fluid Dynamics. 2015; 1(11): 1-24.
[36]. Mavriplis DJ. Accurate multigrid solution of the Eulerequations on unstructured and adaptive meshes. AIAA Journal 1990; 28(2): 213-221.
[37]. Maciel ESG. Simulations in 2D and 3D applying unstructured algorithms, Euler and Navier-Stokes equations – Perfect gas formulation. Saarbrücken, Deutschland: Lambert Academic Publishing (LAP). 2015; Ch. 1: 26-47.
[38]. Maciel ESG. Simulations in 2D and 3D applying unstructured algorithms, Euler and Navier-Stokes equations – Perfect gas formulation. Saarbrücken, Deutschland: Lambert Academic Publishing (LAP). 2015; Ch. 6: 160-181.
[39]. Saxena SK, Nair MT. An improved Roe scheme for real gas flow. AIAA Paper 2005-0587; 2005.
[40]. Gaitonde DV. Development of a solver for 3-D non-ideal magnetogasdynamics. AIAA Paper 99-3610; 1999.
[41]. Hussaini MY, Streett CL, Zang TA. Spectralmethods for partial differential equations. ICASE Report No. 83-46; 1983.
[42]. Davis PA, Rabinowitz P. Numerical integration. Blaisdell Publishing Co.; 1967.
[43]. Canuto C, Hussaini MY, Quarteroni A, Zang TA. Spectral methods evolution to complex geometries and applications to fluid dynamics. Scientific Computation Springer; 2007.
[44]. Prabhu RK. An implementation of a chemical and thermal nonequilibrium flow solver on unstructured meshes and application to blunt bodies. NASA CR-194967; 1994.

[45]. Maciel ESG. Hypersonic reactive flow simulations in two-dimensions, chemical and thermochemical non-equilibrium conditions. Saarbrücken. Deutschland: Lambert Academic Publishing (LAP). 2015; Ch. 3:174-247.
[46]. Maciel ESG. Hypersonic reactive flow simulations in two-dimensions, chemical and thermochemical non-equilibrium conditions. Saarbrücken. Deutschland: Lambert Academic Publishing (LAP). 2015; Ch. 4: 248-332.
[47]. Ait-Ali-Yahia D, Habashi WG. Finite element adaptive method for hypersonic thermochemical nonequilibrium flows. AIAA Journal.1997; 35(8): 1294-1302.
[48]. Long LN, Khan MMS, Sharp HT. Massively parallel three-dimensional Euler / Navier-Stokes method. AIAA Journal. 1991; 29(5): 657-666.
[49]. Vincente WG, Kruger Jr. CH. Introduction to physical gas dynamics. Malabar, Florida, EUA: Krieger Publishing Company. 2002; Ch. 1: 1-26.
[50]. Fox RW, McDonald AT. Introdução à mecânica dos fluidos. Guanabara Editor; 1988.
[51]. Maciel ESG. Simulação numérica de escoamentos supersônicos e hipersônicos utilizando técnicas de dinâmica dos fluidos computacional.DoctoralThesis. ITA, CTA, São José dos Campos, SP, Brazil; 2002.
[52]. Anderson Jr. JD. Fundamentals of aerodynamics. McGraw-Hill, Inc., 5th Edition, 1008p.; 2010.